

# 50. High-Temperature Superconductors

Rainer Wesche

The discovery by J. G. Bednorz and K. A. Müller in 1986 that the superconducting state can exist in oxides at temperatures above 30 K stimulated research in the field of superconductivity and opened a new field of research. Within a few years a large number of cuprate superconductors with transition temperatures well above the boiling point of liquid nitrogen have been found. In this chapter, an overview of the major families of high-temperature superconductors and their physical properties is presented.

Starting from the well-known characteristics of conventional superconductors, described in Sect. 50.1, the new phenomena observed in high-temperature superconductors are considered. The complexity of the physical properties of the cuprate superconductors is closely related to the fact that these materials are close to a metal-insulator transition. In Sects. 50.2 and 50.3, the crystal structures, the general trends for the critical temperatures, the anisotropy of the physical properties, and the factors limiting the transport critical current density are discussed. Because of their importance in the field of electronics some features of thin films are presented in Sect. 50.4.

Strictly speaking, the binary compound  $\text{MgB}_2$  is not a high-temperature superconductor. Nevertheless, an overview of the physical properties of this interesting metallic superconductor, characterized by a transition temperature as high as 39 K, has been included in the present chapter (Sect. 50.5).

In 2008, H. Hosono et al. discovered that the layered superconductor  $\text{La}(\text{O}_{1-x}\text{F}_x)\text{FeAs}$  ( $x = 0.11$ ) superconducts at a temperature as high as 26 K.

50.1	<b>The Superconducting State</b> .....	1228
50.1.1	Characteristic Properties of Superconductors .....	1228
50.1.2	Superconductor Electrodynamics .....	1229
50.1.3	Superconductivity: A Macroscopic Quantum Phenomenon .....	1230
50.1.4	Type II Superconductors .....	1232
50.2	<b>Cuprate High-<math>T_c</math> Superconductors: An Overview</b> .....	1234
50.2.1	Major Families of Cuprate Superconductors .....	1234
50.2.2	Generic Phase Diagram of Cuprate Superconductors .....	1235
50.2.3	Crystal Structures .....	1236
50.2.4	Critical Temperatures .....	1238
50.3	<b>Physical Properties of Cuprate Superconductors</b> .....	1239
50.3.1	Anisotropic Superconductors .....	1239
50.3.2	Irreversibility Line .....	1239
50.3.3	Limitations of the Transport Critical Current .....	1241
50.4	<b>Superconducting Films</b> .....	1244
50.5	<b>The Special Case of <math>\text{MgB}_2</math></b> .....	1245
50.6	<b>Iron-Based Superconductors</b> .....	1248
50.7	<b>Summary</b> .....	1250
	<b>References</b> .....	1252

A maximum critical temperature of 58 K has been reported for the iron-pnictide superconductor  $\text{Sm}(\text{O}_{0.74}\text{F}_{0.26})\text{FeAs}$ . The iron-based superconductors are therefore considered as a second class of high-temperature superconductors. Their properties are described in Sect. 50.6.

After the successful development of helium liquefaction techniques in the laboratory of Heike Kamerlingh Onnes at the University of Leiden, temperatures down to about 1 K became accessible for further research [50.1]. One of the first aspects to be studied was the electrical resistivity of pure metals at very

low temperatures. The nearly temperature-independent residual resistivity of platinum and gold was found to decrease with increasing purity of the metals. In 1911, Kamerlingh Onnes found that, in contrast to the behavior of platinum and gold, the electrical resistivity of mercury drops to an unmeasurably small value at

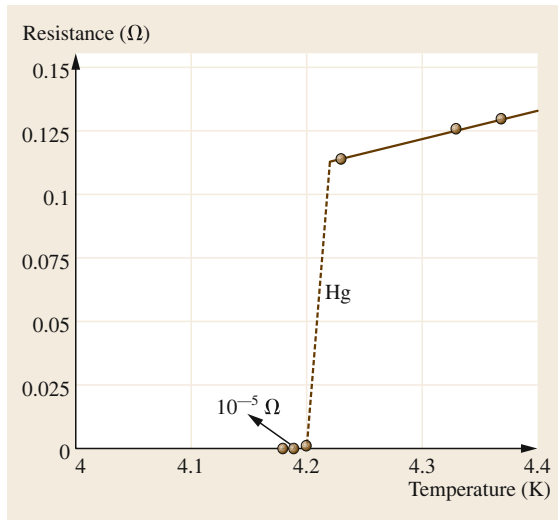


**Fig. 50.1** Resistance–temperature plot for mercury obtained by Heike Kammerlingh Onnes

a temperature of 4.2 K, as shown in Fig. 50.1. The remarkable phenomenon of superconductivity had been discovered [50.1].

In addition to zero resistance, the superconducting state is characterized by perfect diamagnetism. *W. Meissner* and *R. Ochsenfeld* found in 1933 that, as soon as the superconducting state is reached, a magnetic field is expelled from the interior of a superconductor cooled in the presence of a static magnetic field [50.2]. In contrast to the shielding of a magnetic field applied to a material in the superconducting state, field expulsion cannot be explained by perfect conductivity. This Meissner effect is therefore indeed an additional characteristic property of superconductors.

The discoveries listed in Table 50.1 provide an overview of the history of superconductivity. The improvement in the highest known critical temperatures

in metals, oxides, molecular (organic), and iron-based superconductors is shown in Fig. 50.2. Between 1911 and 1974, the critical temperatures  $T_c$  of metallic superconductors steadily increased from 4.2 K in mercury up to 23.2 K in sputtered  $\text{Nb}_3\text{Ge}$  films [50.17, 18].  $\text{Nb}_3\text{Ge}$  held the record for the critical temperature in metallic superconductors until the unexpected discovery of superconductivity at 39 K in the intermetallic compound  $\text{MgB}_2$  [50.15].

The first superconducting oxide  $\text{SrTiO}_3$  characterized by a transition temperature as low as 0.25 K was discovered in 1964 [50.19]. A remarkably higher critical temperature of 13 K was found for the perovskite  $\text{BaPb}_{1-x}\text{Bi}_x\text{O}_3$  in 1975 [50.20]. These results stimulated *J. G. Bednorz* and *K. A. Müller* to search for higher critical temperatures in oxides. Their discovery of high-temperature superconductivity in the cuprate  $(\text{La, Ba})_2\text{CuO}_4$  ( $T_c \approx 30$  K) opened up a new field of research [50.12]. Within less than a year a critical temperature well above the boiling point of liquid nitrogen could be achieved in  $\text{YBa}_2\text{Cu}_3\text{O}_{7-\delta}$  [50.21]. So far, the highest transition temperature of 135 K at ambient pressure has been found in  $\text{HgBa}_2\text{Ca}_2\text{Cu}_3\text{O}_{8+\delta}$  [50.13, 14].

It should be mentioned that the phenomenon of superconductivity has also been observed in organic materials [50.22–24] and fullerenes [50.25–27]. Remarkably, high transition temperatures of 19, 33 and 40 K have been found in the fullerenes  $\text{K}_3\text{C}_{60}$ ,  $\text{RbCs}_2\text{C}_{60}$ , and  $\text{Cs}_3\text{C}_{60}$  respectively.

Since *H. Hosono* and collaborators discovered in 2008 [50.16] that the iron-pnictide  $\text{La}(\text{O}_{0.89}\text{F}_{0.11})\text{FeAs}$  superconducts at a temperature of 26 K, the cuprates are no longer the only known class of complex high-temperature superconductors. The highest reported critical temperatures of iron-based superconductors are in the range of 56–58 K.

An important advantage of high-temperature superconductors is the possibility of operating devices at

**Table 50.1** Milestones in the history of superconductivity

1911	<i>H. Kammerlingh Onnes</i> discovers superconductivity in Hg [50.1]
1933	<i>W. Meissner</i> and <i>R. Ochsenfeld</i> find perfect diamagnetism for the superconducting state [50.2]
1935	London theory of the superconductor electrodynamics [50.3]
1957	<i>J. Bardeen</i> et al. develop a quantum theory of superconductivity (BCS theory) [50.4, 5]
1960	<i>I. Giaever</i> measures the energy gap by electron tunneling [50.6, 7]
1961	Experimental confirmation of flux quantisation indicating the existence of Cooper pairs [50.8, 9]
1962	<i>B. D. Josephson</i> predicts Cooper pair tunneling between two superconductors separated by a thin insulating oxide layer [50.10]
1965	Observation of superconducting quantum interference between Josephson junctions in multiply connected superconducting circuits [50.11]
1986	<i>J. G. Bednorz</i> and <i>K. A. Müller</i> discover high-temperature superconductivity in the La-Ba-Cu-O system [50.12]
1993	Critical temperature of 135 K in $\text{HgBa}_2\text{Ca}_2\text{Cu}_3\text{O}_{8+\delta}$ [50.13, 14]
2001	<i>J. Akimitsu</i> et al. discover superconductivity at 39 K in $\text{MgB}_2$ [50.15]
2008	<i>H. Hosono</i> et al. discover superconductivity at 26 K in the layered iron pnictide $\text{La}(\text{O}_{0.89}\text{F}_{0.11})\text{FeAs}$ [50.16]

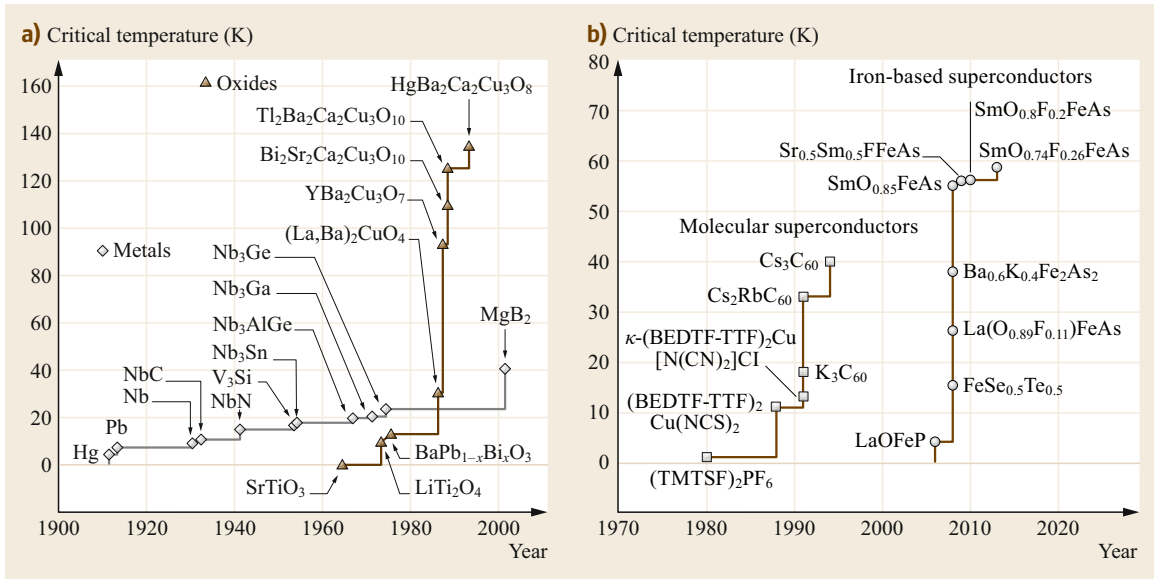


**Fig. 50.2a,b** Highest known critical temperatures of metallic, oxide, molecular (TMTSF and BEDTF-TTF) and iron-based superconductors. Between 1911 and 1974, the critical temperature of metallic superconductors increased steadily from 4.2 K (Hg) to 23.2 K (Nb<sub>3</sub>Ge). In 2001, the unexpected discovery of superconductivity in MgB<sub>2</sub> raised the maximum known  $T_c$  of metallic superconductors to 39 K. After the discovery of high- $T_c$  superconductivity in (La, Ba)<sub>2</sub>CuO<sub>4</sub>, in 1986, the maximum  $T_c$  of oxides rapidly exceeded 77 K the boiling point of liquid nitrogen (a). In 1980, a first molecular superconductor was discovered. In the fullerene Cs<sub>3</sub>C<sub>60</sub>, a remarkably high  $T_c$  of 40 K was found. Between 2006 and 2013, the maximum known  $T_c$  of iron-based superconductors increased from around 4 K (LaOFeP) to 58 K (SmO<sub>0.74</sub>F<sub>0.26</sub>FeAs) (b). (After [50.12–34])

temperatures well above 20 K, leading to a considerable reduction in the required refrigerator input power. In contrast to power applications, the use of liquid nitrogen as a coolant is of less importance for superconducting electronics, which are typically cooled by closed cycle coolers. The economics of closed cycle coolers depends strongly on the operating temperature. Considering an ideal, reversible cooling cycle, the input power necessary to remove a heat load  $dQ/dt$  is

$$P_{\text{in}} = \frac{1}{\eta_c} \frac{dQ}{dt}, \quad (50.1)$$

where

$$\eta_c = \frac{T_{\text{op}}}{300 \text{ K} - T_{\text{op}}} \quad (50.2)$$

is the Carnot efficiency. To remove a heat input of 1 W an ideal, reversible refrigerator consumes at room temperature a power of 70 W for  $T_{\text{op}} = 4.2$  K, whereas this power is only 9 and 2.9 W for operation at 30 and 77 K, respectively. The efficiency  $\eta_r$  of real refrigerators is much smaller than the Carnot efficiency, and depends strongly on the refrigerator size, as illustrated in Fig. 50.3. For small refrigerators able to remove a power of 1 W, the refrigerator efficiency is only a few

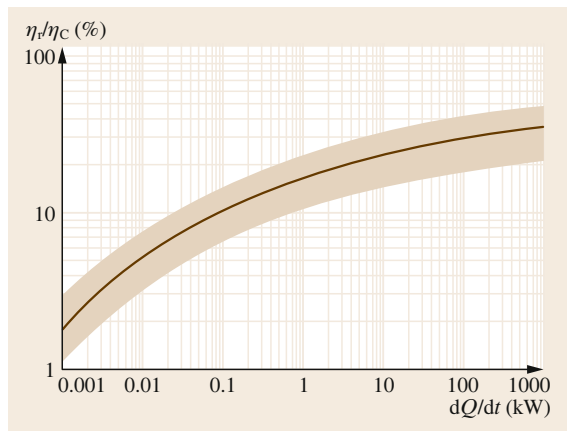


**Fig. 50.3** The efficiency of real refrigerators normalized to the Carnot efficiency is typically in the highlighted area. The ratio of  $\eta_r/\eta_c$  increases with increasing refrigeration capacity. (After [50.35])

percent of the Carnot efficiency. On the other hand, large refrigerators with a cooling capacity well above 10 kW may reach 30% of the Carnot efficiency. The ratio  $\eta_r/\eta_c$  has been found to depend only weakly on the operating temperature.

## 50.1 The Superconducting State

### 50.1.1 Characteristic Properties of Superconductors

The discussion of the physical properties of high-temperature superconductors has to be based on the knowledge of the behavior of conventional, metallic superconductors. In this section the superconducting state is therefore described in more detail, starting from the properties of simple, metallic superconductors.

Below a certain temperature,  $T_c$  the electrical resistance of a superconducting material vanishes. The critical temperature  $T_c$  is characteristic of the superconductor in question. In pure metals, the zero resistance state can be reached within a few mK (Fig. 50.1). In the chemically complex cuprate, high- $T_c$  superconductors the transition to the superconducting state is less sharp than in metallic low- $T_c$  superconductors. The transition width  $\Delta T_c$  for single-phase cuprate superconductors is typically 1 K. Thus the critical temperature depends slightly on the criterion used to define  $T_c$ . Several criteria are illustrated in Fig. 50.4.

At the transition temperature, a resistance drop of several orders of magnitude is typically observed. However, it is in principle not possible to prove experimentally that the resistance in the superconducting state is in fact zero. The most efficient way to determine an upper limit of the resistance is to detect the decay of the magnetic fields generated by currents induced in a su-

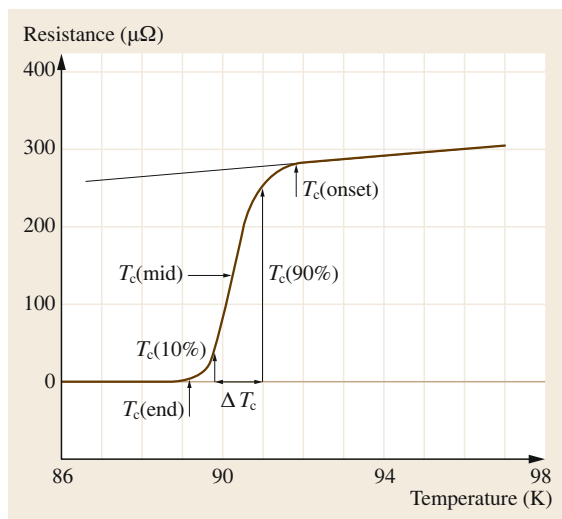


**Fig. 50.4** Resistance versus temperature for a  $\text{Bi}_2\text{Sr}_2\text{CaCu}_2\text{O}_8/\text{Ag}$  multicore wire. The transition temperatures resulting from different definitions of  $T_c$  are indicated. The width of the transition  $\Delta T_c = T_c(90\%) - T_c(10\%)$  is  $\approx 1.2$  K

perconducting loop. Upper resistivity limits between  $2 \times 10^{-18}$  [50.36] and  $7 \times 10^{-23}$   $\Omega$  cm [50.37] have been reported for the high- $T_c$  superconductor  $\text{YBa}_2\text{Cu}_3\text{O}_7$ , while a value of  $3.6 \times 10^{-23}$   $\Omega$  cm has been found for type I low- $T_c$  superconductors [50.38]. These upper resistivity limits are orders of magnitude smaller than the resistivity of  $10^{-10}$   $\Omega$  cm at 4.2 K achievable in annealed, very pure metals. It is therefore justified to assume zero resistance below  $T_c$  for all practical purposes.

The second outstanding feature of the superconducting state is perfect diamagnetism. To understand the magnetic behavior of a superconductor, the two different situations illustrated in Fig. 50.5 have to be considered. In the first case, the superconductor is cooled below  $T_c$  without an applied magnetic field (zero field-cooled). In the second case the superconductor is cooled below  $T_c$  while a magnetic field is applied (field-cooled). In both cases, the magnetic flux is excluded from the interior of the superconductor. Screening currents flowing in the surface layer of the superconductor generate a flux opposite to that of the applied magnetic field. The magnetic flux density is therefore zero everywhere inside the superconductor. On the other hand, outside the superconducting sphere the magnetic field is enhanced because of the superposition of the flux

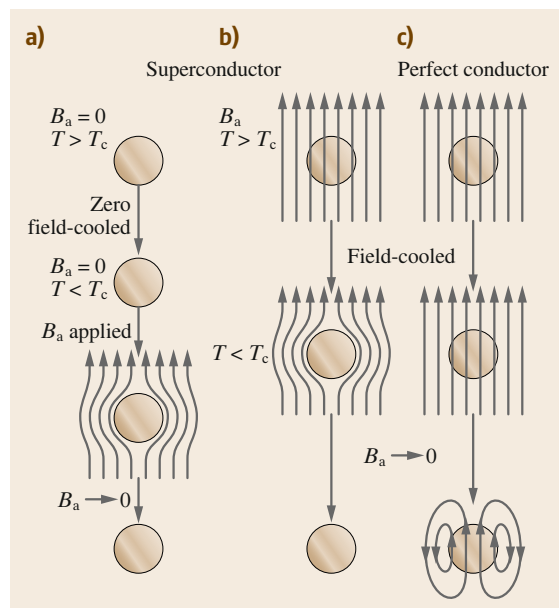


**Fig. 50.5a–c** The magnetic flux is excluded from the interior of a superconductor (a) without field-cooling as well as (b) with it. In contrast to this behavior, a magnetic flux would exist in the interior of a field-cooled perfect conductor (c). (After [50.39, p. 20])

of the applied magnetic field and that of the screening currents. In both situations, the superconductor is unmagnetized when the magnetic field is removed. The behavior of a zero field-cooled superconductor may be considered simply as a screening effect caused by perfect conductivity. In contrast to screening, the expulsion of the magnetic flux from a field-cooled superconductor (the Meissner effect) cannot be explained by perfect conductivity. The different behavior of a field-cooled perfect conductor is also shown in Fig. 50.5. The values of the relative magnetic permeability for nonferromagnetic metals are close to unity. Thus the magnetic flux inside the metal is nearly the same as that of the applied magnetic field. Because  $dB/dt = 0$ , no screening currents are induced, and hence the magnetic flux is not removed from the interior of the perfect conductor at low temperatures. Finally, the removing of the magnetic field ( $dB/dt \neq 0$ ) leads to the magnetization of the perfect conductor.

The superconducting state can be destroyed by a sufficiently large applied magnetic field. The transition from the superconducting to the normal state occurs at a certain critical magnetic field  $B_c$ , which is a characteristic property of the superconductor considered. The dependence of the critical field on the temperature is typically well described by

$$B_c(T) = B_{c0} \left[ 1 - \left( \frac{T}{T_c} \right)^2 \right], \quad (50.3)$$

where  $T_c$  is the critical temperature and  $B_{c0}$  is the critical field at zero temperature. The critical field as a function of temperature is shown in Fig. 50.6 for selected metallic superconductors. The  $B_c(T)$  curves

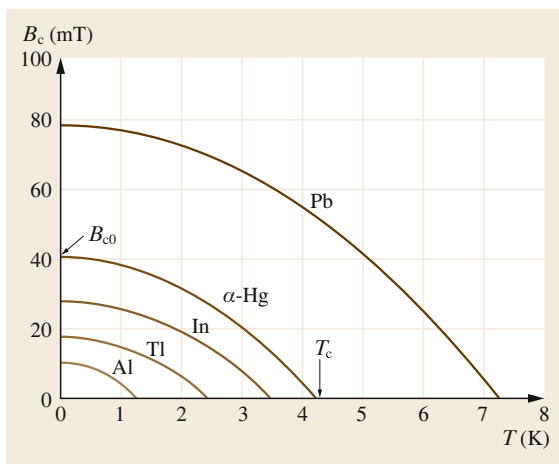


**Fig. 50.6** Critical field versus temperature curves for selected metallic superconductors. The  $B_{c0}$  values vary from  $\approx 10$  to  $\approx 80$  mT. (After [50.39, p. 24])

separate the superconducting from the normal state. The Meissner effect ensures that the properties at any point in the superconducting state are independent of the order in which the final conditions of the applied magnetic field and temperature are reached.

### 50.1.2 Superconductor Electrodynamics

The electrodynamics of superconductors can be described by the two London equations. As a consequence of the infinite conductivity in the superconducting state, Ohm's law must be replaced by the first London equation

$$\frac{d\mathbf{j}}{dt} = \frac{1}{\mu_0 \lambda_L^2} \mathbf{E}, \quad (50.4)$$

where  $\mathbf{j}$  is the current density,  $\mathbf{E}$  is the electric field,  $\mu_0$  is the permeability of free space, and  $\lambda_L$  a constant. The electric field in the superconductor is zero for constant current density. The current density and the magnetic field are related by the second London equation

$$\text{curl} \mathbf{j} = -\frac{1}{\mu_0 \lambda_L^2} \mathbf{B}. \quad (50.5)$$

Using the Maxwell equation  $\text{curl} \mathbf{B} = \mu_0 \mathbf{j}$  the following differential equation results for the magnetic field

$$\nabla^2 \mathbf{B} = \frac{1}{\lambda_L^2} \mathbf{B}. \quad (50.6)$$

For a semi-infinite superconductor with the magnetic field applied along the  $z$ -direction, an exponential decay of the magnetic field  $\mathbf{B}(x) = \mathbf{B}_0 \exp(-x/\lambda_L)$  results, as illustrated in Fig. 50.7. The London penetration depth  $\lambda_L$  is therefore the characteristic length for the decay of the magnetic field in the surface layer of the superconductor. Typical values of the penetration depth are  $10^{-5}$ – $10^{-6}$  cm at  $T = 0$ . The penetration depth is closely related to the number density of the Cooper pairs (Sect. 50.1.3)

$$\lambda_L = \sqrt{\frac{m_C}{\mu_0 n_C q_C^2}}, \quad (50.7)$$

where  $n_C$ ,  $q_C$ , and  $m_C$  are the number density, the charge and the mass of the Cooper pairs. Because of the decreasing Cooper pair density, the penetration depth increases rapidly for temperatures close to  $T_c$  (see the inset of Fig. 50.7). The temperature dependence is given by

$$\lambda_L(T) = \lambda_{L0} \left[ 1 - \left( \frac{T}{T_c} \right)^4 \right]^{-1/2}, \quad (50.8)$$

where  $\lambda_{L0}$  is the penetration depth at  $T = 0$ .

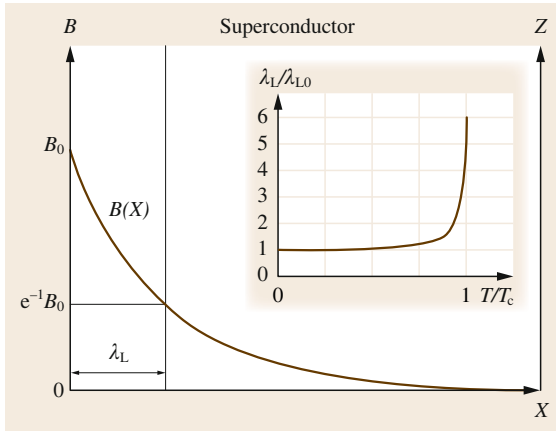


**Fig. 50.7** Exponential decay of an applied magnetic field in the surface layer of a semi-infinite superconductor. The normalized penetration depth  $\lambda_L/\lambda_{L0}$  versus reduced temperature is shown in the inset

### 50.1.3 Superconductivity: A Macroscopic Quantum Phenomenon

#### Bardeen–Cooper–Schrieffer (BCS) Theory

Next, the microscopic causes of superconductivity in conventional superconductors are briefly described. *J. Bardeen* et al. proposed a microscopic theory of superconductivity [50.4, 5], which is now well known as the BCS theory. At the moment, it seems to be unlikely that the mechanism of superconductivity in the cuprates, which is still not yet understood, can be explained by the BCS theory. The recently discovered iron-based superconductors seem to be a second class of high-temperature superconductors, which show unconventional superconductivity [50.16]. In this chapter, only some fundamental ideas and results of the BCS theory are presented.

Independent of each other, two researchers [50.40, 41] found theoretically that lattice vibrations (phonons) can provide an attractive interaction between two electrons. This can be understood as a consequence of the polarization of the lattice by the electrons. The concentration of positive charges produced by the first electron reduces the potential energy of the second electron. Because of this attractive interaction, electrons with opposite momenta and spins form electron (Cooper) pairs. The Cooper pairs, characterized by zero spin and momentum, have to be considered as new particles. Because their spin is zero, they do not obey Pauli's exclusion principle. The probability that a state is occupied increases with the number of particles populating the same quantum state. Therefore, all Cooper pairs occupy the same quantum state with a single value of the momentum in the presence of an applied electric

field. A change of momentum results only for scattering processes that break up some Cooper pairs. Resistance occurs as soon as the energy taken from the electric field exceeds the binding energy of the Cooper pairs. This behavior explains the existence of a critical current.

The electron–phonon interaction leads to an energy gap  $2\Delta$  in the density of states for the single electrons. The width of the energy gap at zero temperature is

$$2\Delta(0) = 3.5k_B T_c, \quad (50.9)$$

where  $k_B$  is the Boltzmann constant and  $T_c$  is the critical temperature. For superconducting elements the measured ratios of  $2\Delta(0)/k_B T_c$  are typically 3.2–4.6 [50.42], which is in reasonably good agreement with the value of 3.5 predicted by the BCS theory. The single-electron density of states close to the Fermi energy is

$$D_s(E - E_F) = D_n(E_F) \frac{|E - E_F|}{\sqrt{(E - E_F)^2 - \Delta^2}}, \quad (50.10)$$

where  $\Delta$  is the half-width of the energy gap and  $|E - E_F| > \Delta$ . The variation of the normal state density of states  $D_n(E)$  can be neglected because  $E_F \gg 2\Delta$ . The single-electron density of states shown in Fig. 50.8 reflects that the energy states present in the normal state within the energy gap are shifted to the edges. The inset of Fig. 50.8 shows the temperature dependence of the energy gap predicted by the BCS theory. The critical temperature is [50.5]

$$T_c = 1.14 \frac{\hbar\omega_D}{k_B} \exp\left(-\frac{1}{D_n(E_F)V_p}\right), \quad (50.11)$$

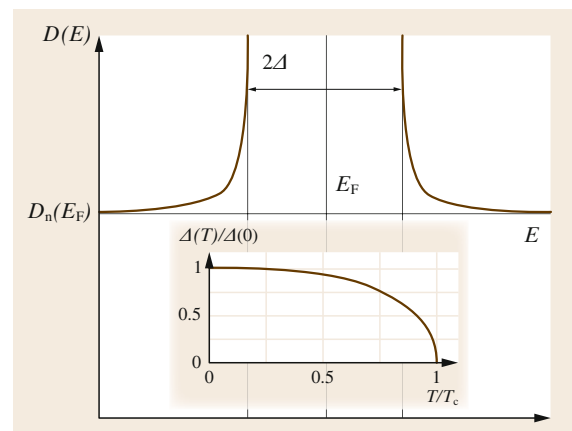


**Fig. 50.8** Energy gap and density of states for unpaired electrons in the superconducting state in the vicinity of the Fermi energy  $E_F$ . The temperature dependence of the energy gap predicted by the BCS theory is shown in the inset

where the electron–phonon interaction is described by the constant  $V_p$ . The Debye frequency  $\omega_D$  is the cut-off frequency of the phonon spectrum in a solid. Considering the atoms in a solid as harmonic oscillators of frequency  $\omega = (k_e/M)^{1/2}$ , where  $k_e$  is the elastic constant resulting from the binding forces, both  $\omega_D$  and  $T_c$  are expected to be proportional to  $M^{-1/2}$  for different isotopes of the same element. In many metallic superconductors, this isotope effect has been observed [50.43–46].

All Cooper pairs populate the same quantum state, resulting in a collective wave function

$$\psi = n_C^{1/2} \exp[i\varphi(r)], \quad (50.12)$$

where  $n_C = \psi^* \psi$  ( $\psi^*$ : conjugate complex of  $\psi$ ) is their concentration. Because the phase coherence of the Cooper pairs is effective at large distances, the phase  $\varphi(r)$  is a macroscopically observable quantity. As a consequence, the magnetic flux in a superconducting hollow cylinder of the cross-sectional area  $F$  is quantized

$$\phi = \int_F B dF = \frac{h}{2e} N_\phi = \phi_0 N_\phi. \quad (50.13)$$

In the above equation,  $N_\phi$  is an integer,  $e$  is the electron charge and  $\phi_0 = 2.068 \times 10^{-15}$  V s is the flux quantum. The magnetic flux generated by the screening currents flowing in the surface layer of the superconductor is typically small, and has therefore been neglected.

### Tunneling Effects

First, single-electron tunneling in a normal–insulator–superconductor (N-I-S) junction will be considered. The two conductors are separated by an insulating oxide layer typically less than 2 nm thick. Tunneling can take place only when empty target energy states are available, otherwise the process is forbidden by the Pauli principle (Fig. 50.9). For a voltage of  $U = \Delta/e$  ( $-e > 0$ ), the empty energy states of the superconductor above the energy gap reach the same level as the Fermi energy of the normal conductor, and strong tunneling sets in. On the other hand, for a voltage  $U = -\Delta/e$ , pair breaking becomes possible. One of the electrons tunnels into the normal conductor and gains an energy  $\Delta$  available for the excitation of the second electron to an empty state above the energy gap. The resulting N-I-S current–voltage characteristic and the Bose condensation representation of the tunneling process are shown in Fig. 50.9.

In the case of two identical superconductors (S-I-S junction), strong single-electron tunneling sets in at an applied voltage  $|U| \geq |2\Delta/e|$ . This voltage is high

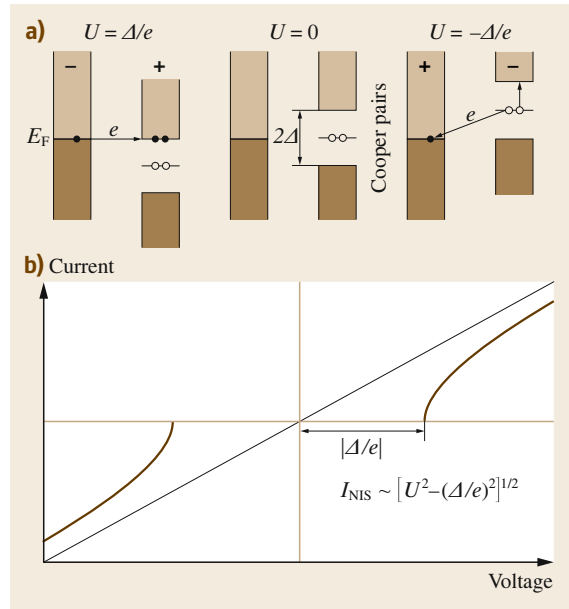


**Fig. 50.9a,b** Bose condensation representation of N-I-S tunneling (a) and the corresponding current voltage characteristic at  $T = 0$  (b)

enough to allow the empty energy states above the gap of the first superconductor, and the filled energy states below the gap of the second superconductor, to overlap; pair breaking becomes possible. Figure 50.10 shows the semiconductor representation of the tunneling process and the resulting S-I-S current–voltage characteristic. The weak tunneling currents for  $|U| < |2\Delta/e|$  are a consequence of a few quasi-particles being thermally excited above the energy gap for  $T > 0$  (Fig. 50.10).

So far, only single-electron tunneling has been considered. In 1962, *B. D. Josephson* predicted that Cooper pair tunneling through a very thin insulating layer is possible [50.10]. Even for zero voltage across the insulating layer of an S-I-S junction, Cooper pairs can tunnel through the barrier. This process has to be considered as the tunneling of the wave function collectively describing the Cooper pairs. The DC current through the contact is

$$I = I_c \sin \delta, \quad (50.14)$$

where  $I_c$  is the critical current of the Josephson junction. The Josephson DC current through the contact is between  $-I_c$  and  $I_c$ , depending on the phase difference  $\delta$  of the two Cooper pair wave functions. This phase difference is time independent for zero voltage across the insulating layer. Applying a DC voltage  $U$  across the insulating layer of the Josephson contact causes a time-

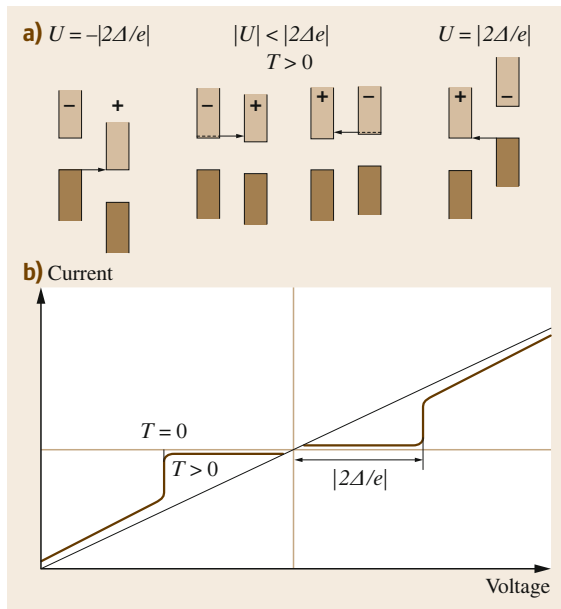


**Fig. 50.10a,b** S-I tunneling. The semiconductor representation of the process (a) shows that strong tunneling sets in for  $U = |2\Delta/e|$ . A few electrons (quasi particles) are thermally excited into states above the gap at  $T > 0$ . The corresponding current–voltage characteristic (b) shows that these electrons are responsible for the weak tunneling current at low voltages. (After [50.39, p. 42])

dependent phase difference between the two Cooper pair wave functions. As a consequence, there flows an AC current

$$I_{AC} = I_c \sin [2\pi\nu_J t + \delta(0)], \quad (50.15)$$

where

$$\nu_J = \frac{2|e|U}{h} = \frac{U}{\phi_0}. \quad (50.16)$$

The AC Josephson current  $I_{AC}$  oscillates with a frequency of 483.6 MHz/ $\mu$ V. The tunneling of the Cooper pair through the barrier is connected to the emission or absorption of a photon with energy  $E = h\nu_J$ . The AC Josephson current flows in addition to the current resulting from single-electron tunneling. A more detailed description of the AC Josephson effect can be found in [50.42].

Finally, macroscopic quantum interference effects in Josephson junctions will be briefly considered. These interference effects are closely connected to the phase shifts of the Cooper pair wave functions caused by a magnetic field applied transversely to the current direction. The applied magnetic field gives rise to a spatial variation of the phase difference of the two Cooper

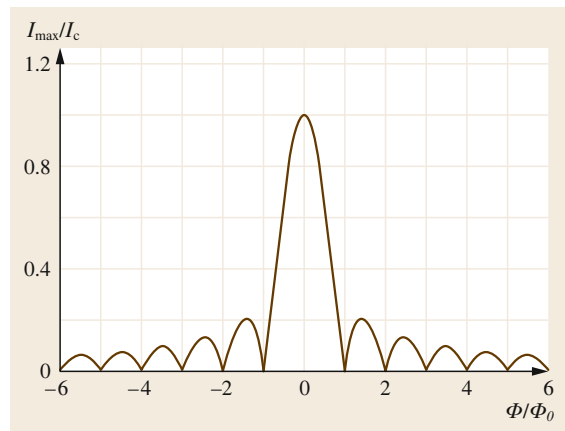


**Fig. 50.11** Josephson–Fraunhofer diffraction pattern for the normalized maximum Josephson DC current  $I_{\max}/I_c$ . Minima of the current occur for  $\Phi/\Phi_0$  values of 1, 2, 3 etc. (After [50.39, p. 49])

wave functions within the contact area. The resulting Josephson DC current for a rectangular barrier is

$$I = I_c \sin \delta_0 \frac{\sin \pi\phi/\phi_0}{\pi\phi/\phi_0}, \quad (50.17)$$

where  $I_c$  is the critical current of the Josephson junction,  $\phi$  is the total flux enclosed by the barrier, and  $\phi_0$  the flux quantum. The phase shift  $\delta_0$  is unknown. The maximum Josephson DC current

$$I_{\max} = I_c \left| \frac{\sin \pi\phi/\phi_0}{\pi\phi/\phi_0} \right| \quad (50.18)$$

is reached for  $\sin \delta_0 = 1$ , corresponding to a phase difference of  $\pi/2$ . In Fig. 50.11, the resulting interference pattern for the Josephson DC current is shown. The Josephson–Fraunhofer interference of the two Cooper pair wave functions indicates that superconductivity is a macroscopic quantum phenomenon (for more details see [50.39]).

#### 50.1.4 Type II Superconductors

A quantitative description of the behavior of type II superconductors is provided by the Ginzburg–Landau theory (see for example [50.42]). In the London theory, the Cooper pair density is assumed to be constant. The only characteristic length scale is the penetration depth  $\lambda_L$  describing the decay of a magnetic field inside a superconductor. Taking into consideration, a variation of the Cooper pair density leads to a second characteristic length scale, namely the coherence length  $\xi$ , the shortest distance within which a considerable change



**Table 50.2** Coherence length  $\xi$  and Ginzburg–Landau parameter  $\kappa$  for selected superconductors at  $T = 0$ . (After [50.39, p. 70])

Material	$T_c$ (K)	$\xi$ (nm)	$\kappa = \lambda_L/\xi$	Reference
Al	1.18	550	0.03	[50.42]
In	3.41	360	0.11	[50.42]
Cd	0.52	760	0.14	[50.42]
Sn	3.72	180	0.23	[50.42]
Ta	4.5	93	0.38	[50.47]
Pb	7.2	82	0.48	[50.42]
Nb	9.25	39	1.28	[50.42]
NbTi	9.5	4	75	[50.48]
Nb <sub>3</sub> Sn	18	3	21.7	[50.48]
Nb <sub>3</sub> Ge	23.2	3	30	[50.48]
Rb <sub>3</sub> C <sub>60</sub>	29.6	2	123.5	[50.49]
YBa <sub>2</sub> Cu <sub>3</sub> O <sub>7-<math>\delta</math></sub>	93	2	95	[50.42]

of the Cooper pair density can occur. At the interface of a normal and a superconductor, the Cooper pair density increases continuously from zero to the value  $n_C$  deep inside the superconductor. The ratio of the coherence length and the penetration depth is the Ginzburg–Landau parameter  $\kappa$

$$\kappa = \frac{\lambda_L}{\xi}. \quad (50.19)$$

Depending on whether the parameter  $\kappa$  is smaller or larger than  $1/\sqrt{2}$ , the superconductor in question is of type I or II, respectively. Values of the coherence length and the Ginzburg–Landau parameter of selected metallic superconductors are listed in Table 50.2. The cuprate high- $T_c$  superconductors are extreme type II superconductors with  $\kappa$  values of  $\approx 100$ .

In Fig. 50.12, the phase diagrams of both types of superconductors are compared. In type I superconductors, there exist two different phases, namely the

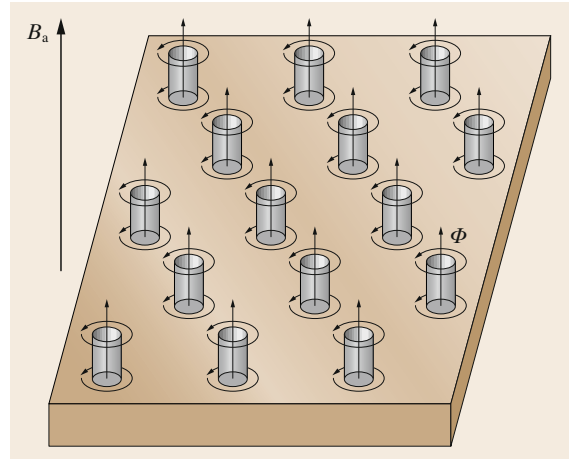


**Fig. 50.13** Type II superconductor in the mixed state. Each vortex contains just a single fluxoid  $\Phi_0 = h/2|e|$ . (After [50.39, p. 74])

superconducting and the normal, which cannot coexist. On the other hand, three different phases can exist in type II superconductors. Below the lower critical field  $B_{c1}(T)$ , the type II superconductor is in the superconducting phase characterized by perfect diamagnetism, where it behaves like a type I superconductor. Above the upper critical field  $B_{c2}(T)$ , the material is in the normal state. In the mixed state between the lower and upper critical fields superconducting and normal regions can coexist in a type II superconductor. The mixed state shown in Fig. 50.13 is characterized by an array of normal cores within the superconductor, which allows magnetic flux to enter into the superconductor. The supercurrents encircling the normal cores (vortices) cause a repulsive vortex–vortex interaction.

In the mixed state of a type II superconductor, the transport currents can flow throughout the conductor. In the presence of a magnetic field perpendicular to

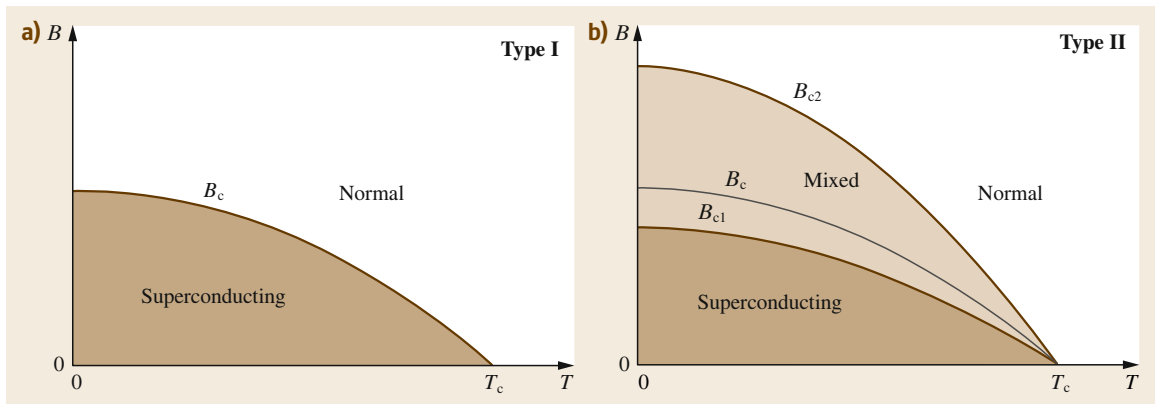


**Fig. 50.12a,b** Comparison of the phase diagrams for type I (a) and II superconductors (b). (After [50.39, p. 74])

the current direction, a Lorentz force  $F_L = j\phi_0$  acts on the vortices, which leads to a motion of the vortices perpendicular to the current and the field direction. The variation of the magnetic flux leads to a flux flow resistance, and hence the critical current would be

zero. However, in a real type II superconductor defects are always present, which act as pinning centers. As long as the Lorentz force is smaller than the pinning force, flux motion is suppressed, resulting in zero resistance.

## 50.2 Cuprate High- $T_c$ Superconductors: An Overview

### 50.2.1 Major Families of Cuprate Superconductors

At present, around 100 cuprate superconductors are known. The major families of cuprate superconductors are listed in Table 50.3. Common features of the cuprate superconductors are layered crystal structures. In the cuprates, conducting copper oxide blocks and insulating charge-carrier reservoirs alternate with each other along the crystallographic  $c$  direction. As a consequence of the layered structures, the physical properties of the cuprates are highly anisotropic. The electrical resistivity along the crystallographic  $a$ - and  $b$ -directions within the conductive  $\text{CuO}_2$  planes is much lower than along the  $c$ -direction, where the current has to cross the insulating charge-carrier reservoirs. Figure 50.14 shows as an example the layering scheme of  $\text{Tl-}22(n-1)n$  superconductors. The three thallium-based compounds are distinguished by the different number  $n$  of  $\text{CuO}_2$  planes in the copper oxide blocks. In the compounds with  $n \geq 2$ , adjacent  $\text{CuO}_2$  planes are separated by Ca layers. In the  $\text{Bi-}22(n-1)n$  counterparts, Tl and Ba are replaced by Bi and Sr, respectively. In both families of cuprate superconductors the copper oxide blocks are embedded between  $\text{TlO}$  or  $\text{BiO}$  double layers. An analogous layering scheme results for the  $\text{Tl-}12(n-1)n$  compounds. However, the copper oxide blocks of these compounds are separated only by single  $\text{TlO}$  layers. The highest critical temperature is typically reached in the com-

pounds with three  $\text{CuO}_2$  layers ( $n = 3$ ) in the copper oxide blocks.

The physical properties of the cuprate superconductors depend strongly on their chemical composition and the resulting carrier concentration. As in semiconductors, the carrier concentration in the cuprates can be changed by doping. For example, let us consider the superconductor  $\text{La}_{2-x}\text{Sr}_x\text{CuO}_4$ . The possible oxidation states of copper are +1, +2, and +3. In the insulating parent compound  $\text{La}_2\text{CuO}_4$ , the oxidation state of copper is +2. The valence of La is +3 and that of Sr +2. Substitution of  $\text{Sr}^{2+}$  for  $\text{La}^{3+}$  leads to the formation of  $\text{Cu}^{3+}$  or  $\text{O}^-$  defects (holes), which are expected to be mobile. Thus, an increasing number of holes is created in the  $\text{CuO}_2$  planes with increasing Sr concentration  $x$ .

The cuprates are complex nonstoichiometric oxides. Heat treatments in reducing or oxidizing atmosphere

**Table 50.3** Major families of superconducting cuprates. (After [50.39, p. 79])

Family	Symbol	Maximum $T_c$ (K)
$(\text{La}_{1-x}\text{M}_x)_2\text{CuO}_4^a$	La-214	39
$\text{YBa}_2\text{Cu}_3\text{O}_7^b$	Y-123	92
$\text{YBa}_2\text{Cu}_4\text{O}_8$	Y-124	80
$\text{Bi}_2\text{Sr}_2\text{Ca}_{n-1}\text{Cu}_n\text{O}_{2n+4}$	$\text{Bi-}22(n-1)n$	122
$\text{Tl}_2\text{Ba}_2\text{Ca}_{n-1}\text{Cu}_n\text{O}_{2n+4}$	$\text{Tl-}22(n-1)n$	128
$\text{TlM}_2\text{Ca}_{n-1}\text{Cu}_n\text{O}_{2n+3}^a$	$\text{Tl-}12(n-1)n$	122
$\text{HgBa}_2\text{Ca}_{n-1}\text{Cu}_n\text{O}_{2n+2}$	$\text{Hg-}12(n-1)n$	135

<sup>a</sup> M = Sr or Ba, <sup>b</sup> Y can be replaced by rare-earth elements

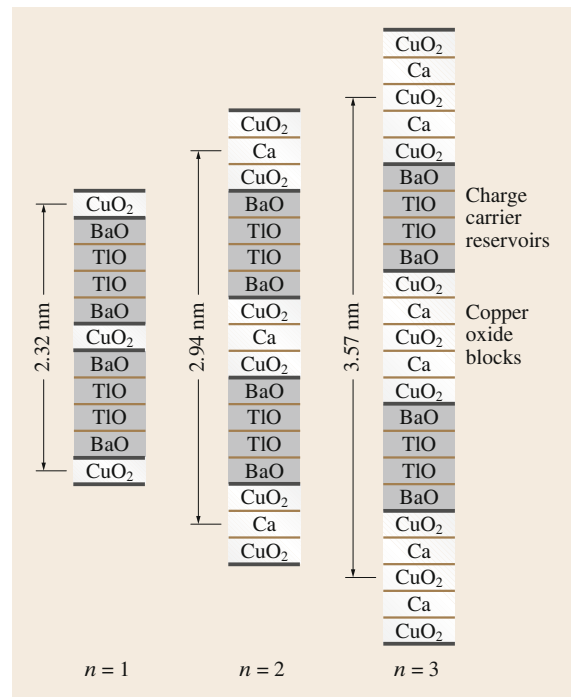
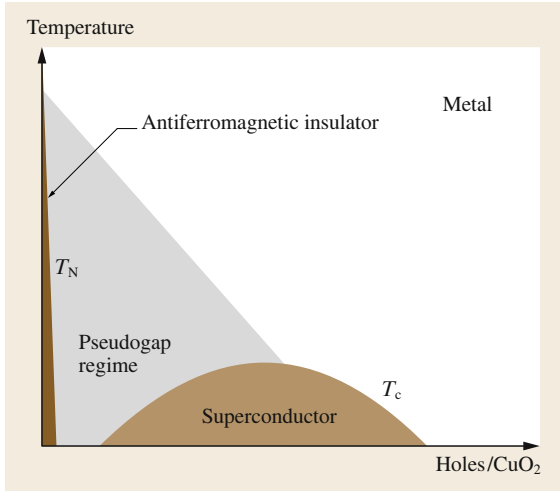


**Fig. 50.14** Layering scheme of  $\text{Tl}_2\text{Ba}_2\text{Ca}_{n-1}\text{Cu}_n\text{O}_{2n+4}$  superconductors. (After [50.39, p. 81])



therefore lead to considerable changes in the oxygen content. Incorporation of excess oxygen is a further way to enhance the hole concentration in the  $\text{CuO}_2$  planes of the cuprates.

Finally, it should be noted that, in addition to the major families of cuprate superconductors listed in Table 50.3, there exist a large number of high-temperature superconductors which can be synthesized only under high pressure (see for example [50.39]).

### 50.2.2 Generic Phase Diagram of Cuprate Superconductors

It is beyond the scope of this chapter to discuss all the new physical phenomena related to cuprate superconductors. To give an impression of the complexity of these materials, the generic phase diagram is briefly

**Fig. 50.15** Generic phase diagram for cuprate superconductors indicating that these materials are close to a metal–insulator transition. The physical properties of the cuprates vary considerably with increasing hole concentration ◀

described. The one shown in Fig. 50.15 indicates that the cuprate superconductors are close to a metal–insulator transition. Their parent compounds are antiferromagnetic Mott insulators, of which  $\text{La}_2\text{CuO}_4$  and  $\text{YBa}_2\text{Cu}_3\text{O}_6$  are examples. The Néel temperature  $T_N$ , at which magnetic ordering sets in, reaches values of 250–400 K in the parent compounds. The Néel temperature decreases rapidly with increasing hole concentration. A transition from an insulating to a superconducting phase is observed for further enhanced doping levels. The critical temperature increases with increasing number of holes and reaches a maximum at  $\approx 0.18$  holes per  $\text{CuO}_2$  unit before decreasing again. At doping levels well above 0.3 holes/ $\text{CuO}_2$ , the material behaves as a nonsuperconducting metal.

In the last few years it could be clarified that the energy gap in cuprate superconductors is of d-wave symmetry, whereas it is of s-wave symmetry in conventional superconductors. The two different symmetries are illustrated in Fig. 50.16. For s-wave symmetry, the superconducting energy gap is constant irrespective of the direction of the wave vector  $\mathbf{k}$ . In the case of d-wave symmetry, there exist positions on the Fermi surface for which the energy gap is zero. At these positions, the sign of the order parameter changes from + to – or vice versa. As a consequence, a finite tunnel conductivity [ $dI/dV \propto D(E)$ ] is observed within the energy gap (Fig. 50.16).

Next, let us consider the temperature dependence of the energy gap. The tunneling conductance of under-

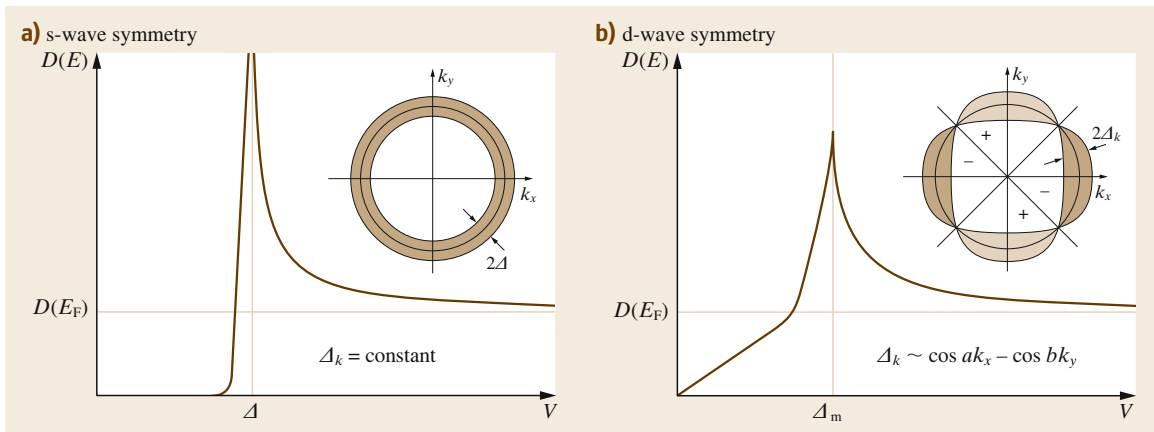


**Fig. 50.16a,b** The two different symmetries of the energy gap and the corresponding density of states. For s-wave symmetry (a), the width of the energy gap is independent of the wave vector  $\mathbf{k}$ . In the case of the d-wave symmetry (b), the energy gap depends on the wave vector. At four positions on the Fermi surface, the energy gap is zero. (After [50.50])

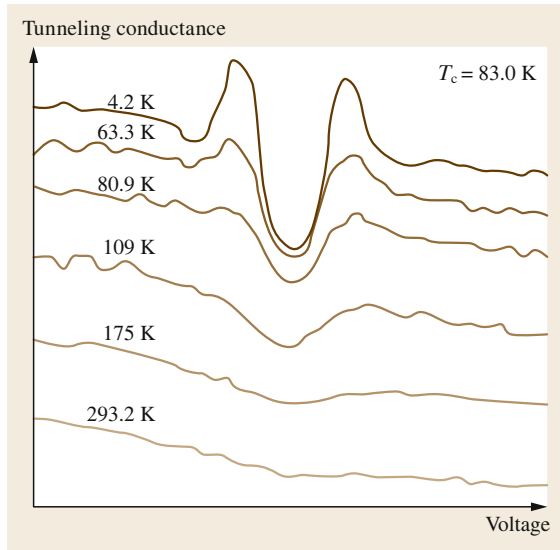


**Fig. 50.17** Schematic illustration of the tunneling conductance of under-doped Bi-2212 providing the density of states in the vicinity of the energy gap. For clarity the spectra are offset vertically. A gap-like feature (pseudogap) can be observed even at a temperature as high as 175 K, well above  $T_c$ . (After [50.51])

doped Bi-2212 as shown in Fig. 50.17 indicates that the energy gap of cuprate superconductors is independent of temperature. This behavior is in contrast to the predictions of the BCS theory. In under-doped cuprate superconductors, the energy gap has been found to increase for decreasing number of charge carriers in spite of a reduced critical temperature. On the other hand, both the energy gap and the critical temperature of over-doped cuprates decrease with increasing carrier concentration. An outstanding feature of cuprate superconductors is the existence of an energy gap even at temperatures well above  $T_c$ . This pseudogap is found in the region of the phase diagram where a transition from an antiferromagnetic insulator to a superconductor occurs.

A potential explanation for the existence of the pseudogap is the formation of Cooper pairs at temperatures well above  $T_c$ . However, because of the low Cooper pair density, they are not macroscopically correlated. As a consequence, the material is not able to carry a supercurrent above  $T_c$ .

The Nernst effect is a thermo-magnetic phenomenon, in which a transverse voltage originates from a transverse magnetic field and a thermal gradient along the sample. In the presence of vortices, the Nernst effect is strongly enhanced. Measurements of the Nernst effect [50.52, 53] provided evidence for pairing well above the critical temperature in under-doped cuprate superconductors. However, the maximum temperature

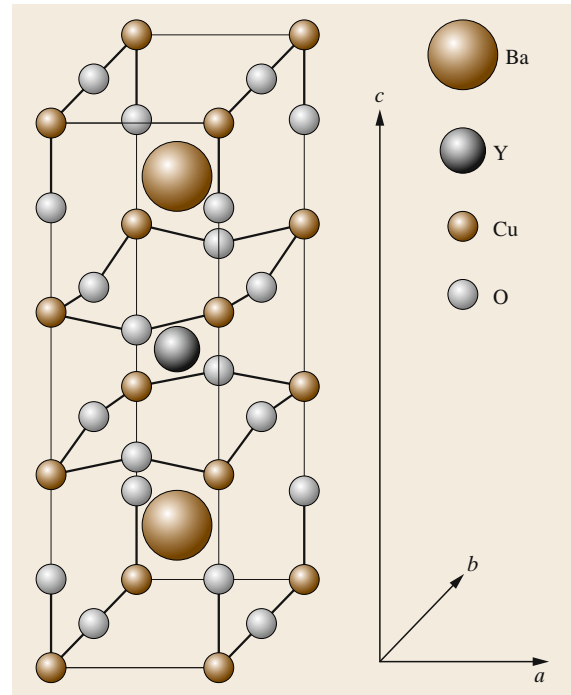


**Fig. 50.18** Orthorhombic unit cell of  $\text{YBa}_2\text{Cu}_3\text{O}_{7-\delta}$ . A special feature of this cuprate are CuO chains in the  $b$ -direction. (After [50.39, p. 100])

for the existence of vortices seems to be well below the temperature at which the pseudogap vanishes.

Newer results seem to favor the hypothesis that the pseudogap phenomenon competes with the gaps associated with superconductivity. A combined scanning tunneling microscopy and angle-resolved photoemission study of  $\text{Bi}_2\text{Sr}_{2-x}\text{La}_x\text{Cu}_{6+\delta}$  showed two distinct energy gaps. In the nodal direction, a small gap was found, which vanished at the critical temperature, while in the anti-nodal direction a large one was observed to exist well above the critical temperature. The two gaps seem to coexist in the antinodal direction [50.54]. In the nodal direction the energy gap of a d-wave superconductor vanishes.

New theories have predicted competing orders in the pseudogap regime of under-doped cuprate superconductors. As an example, let us consider charge stripes. Spin and charge are separated, resulting in antiferromagnetic domains and charge stripes located at the antiphase boundaries [50.55]. Experimental evidence for this scenario has been found from neutron scattering [50.56].

### 50.2.3 Crystal Structures

Next, let us consider the crystal structures of the cuprates in more detail. For  $\text{YBa}_2\text{Cu}_3\text{O}_{7-\delta}$  (Y-123)

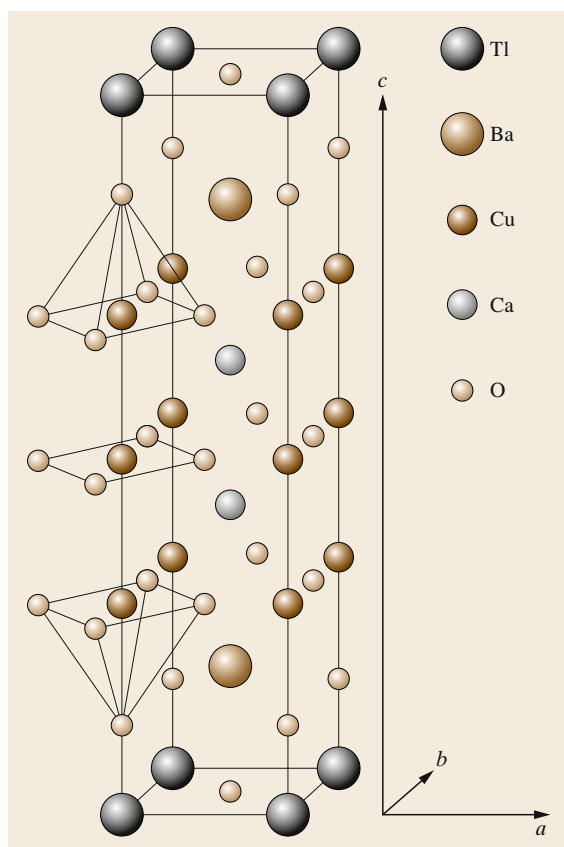


**Fig. 50.19** Primitive tetragonal unit cell of  $\text{TlBa}_2\text{Ca}_2\text{Cu}_3\text{O}_9$ . (After [50.39, p. 108])

an orthorhombic structure with lattice parameters  $a = 0.38$  nm,  $b = 0.39$  nm and  $c = 1.17$  nm has been deduced from x-ray powder diffraction data [50.57, 58]. Figure 50.18 shows the orthorhombic unit cell of Y-123. The unit cell of  $\text{YBa}_2\text{Cu}_3\text{O}_{7-\delta}$  contains double  $\text{CuO}_2$  layers with embedded yttrium ions (Fig. 50.18). Slightly different  $z$  positions of the Cu and O atoms lead to buckling in the  $\text{CuO}_2$  planes. The oxygen atoms occupy perovskite-like anion positions halfway between the copper atoms. These square-coordinated  $\text{CuO}_2$  layers are a characteristic feature of all cuprate superconductors. Because metallic conductivity has been found in these layers, they are also called conduction planes. Along the crystallographic  $c$ -axis perpendicular to these planes, insulating or semiconducting behavior is frequently observed. Neighboring  $\text{CuO}_2$  blocks are separated by two BaO layers. The CuO chains between the two BaO layers in the  $b$ -direction are a special feature of the Y-123 compound.

The crystal structures of  $\text{Tl-}12(n-1)n$  and the analogous  $\text{Hg-}12(n-1)n$  superconductors are primitive tetragonal. Because of the common  $\text{CuO}_2$  planes, the  $a$  and  $b$  lattice parameters of cuprate superconductors are generally close to 0.39 nm. In both cuprate superconductor families, the  $c$  lattice parameter is given approximately by  $c \cong (0.63 + 0.32n)$  nm. As an example of these crystal structures the primitive tetragonal unit cell of  $\text{TlBa}_2\text{Ca}_2\text{Cu}_3\text{O}_9$  is shown in Fig. 50.19. The copper oxide blocks of the Tl-1223 compound are formed of three  $\text{CuO}_2$  layers. The  $\text{CuO}_2$  layers within the copper oxide blocks are separated by

**Table 50.4** Lattice parameters of selected cuprate superconductors. (After [50.39, p. 118])

Compound	Symmetry	$a$ (nm) $b$ (nm)	$c$ (nm)
$\text{La}_{1.85}\text{Sr}_{0.15}\text{CuO}_4$	Tetragonal	0.3779	1.3200
$\text{YBa}_2\text{Cu}_3\text{O}_{6.9}$	Orthorhombic	0.3822 0.3891	1.1677
$\text{Bi}_{2.2}\text{Sr}_2\text{Ca}_{0.8}\text{Cu}_2\text{O}_{8+\delta}^a$	Orthorhombic	0.5414 0.5418	3.089
$(\text{Bi, Pb})_2\text{Sr}_{1.72}\text{Ca}_2\text{Cu}_3\text{O}_{10+\delta}^a$	Orthorhombic	0.5392 0.5395	3.6985
$\text{Tl}_{1.7}\text{Ba}_2\text{Ca}_{1.06}\text{Cu}_{2.32}\text{O}_{8+\delta}$	Tetragonal	0.3857	2.939
$\text{Tl}_{1.64}\text{Ba}_2\text{Ca}_{1.87}\text{Cu}_{3.11}\text{O}_{10+\delta}$	Tetragonal	0.3822	3.626
$\text{Tl}_2\text{Ba}_2\text{Ca}_3\text{Cu}_4\text{O}_{12-\delta}$	Tetragonal	0.3850	4.1984
$\text{Tl}_{1.1}\text{Ba}_2\text{Ca}_{0.9}\text{Cu}_{2.1}\text{O}_{7.1}$	Tetragonal	0.3851	1.2728
$\text{Tl}_{1.1}\text{Ba}_2\text{Ca}_{1.8}\text{Cu}_{3.0}\text{O}_{9.7}$	Tetragonal	0.3843	1.5871
$\text{TlBa}_2\text{Ca}_3\text{Cu}_4\text{O}_{11}$	Tetragonal	0.3848	1.9001
$\text{HgBa}_2\text{CuO}_{4+\delta}$	Tetragonal	0.380	0.9509
$\text{HgBa}_2\text{CaCu}_2\text{O}_{6+\delta}$	Tetragonal	0.3859	1.2657
$\text{HgBa}_2\text{Ca}_2\text{Cu}_3\text{O}_{8+\delta}$	Tetragonal	0.3853	1.5818
$\text{HgBa}_2\text{Ca}_3\text{Cu}_4\text{O}_{10+\delta}$	Tetragonal	0.3854	1.9006

<sup>a</sup> Using a pseudo-tetragonal unit cell a lattice parameter  $a$  (tetragonal)  $\cong (a + b)/2\sqrt{2} \approx 0.38$  nm would result

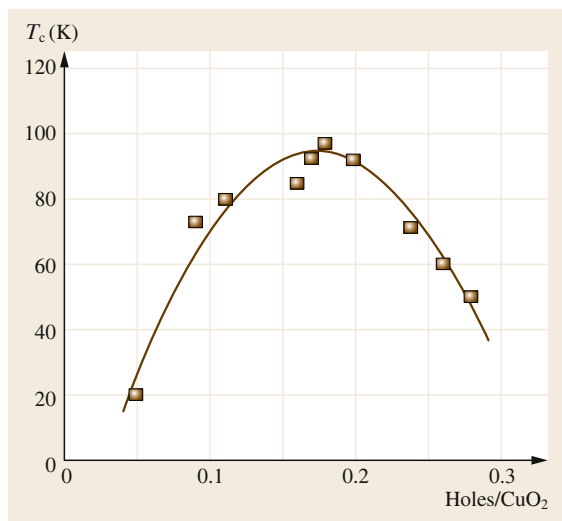


**Fig. 50.20** Critical temperature of  $\text{HgBa}_2\text{CuO}_{4+\delta}$  versus hole concentration. The maximum critical temperature is reached for a hole concentration of 0.18 holes/ $\text{CuO}_2$ . (After [50.39, p. 123], results from [50.59])

**Table 50.5** Critical temperatures of optimally doped cuprate superconductors

Compound	$n$	$T_c$ (K)	Reference
Y-123	2	92	[50.21]
Bi-2212	2	96	[50.60]
Bi-2223	3	122	[50.61]
Tl-2201	1	92	[50.62]
Tl-2212	2	118	[50.62]
Tl-2223	3	128	[50.63]
Tl-2234	4	119	[50.61]
Tl-1212	2	90	[50.61]
Tl-1223	3	122	[50.61]
Tl-1234	4	122	[50.61]
Tl-1245	5	110	[50.61]
Hg-1223	3	135	[50.14]

Ca ions. In contrast to the  $\text{Tl-}22(n-1)n$  compounds (Fig. 50.14) adjacent  $\text{CuO}_2$  blocks are separated by only a single TlO layer. Like the TlO double layers of the  $22(n-1)n$  compounds, the single TlO layers of the  $12(n-1)n$  compounds are embedded between two BaO layers. The reduced distance of neighboring copper oxide blocks leads to an enhanced coupling of the conduction planes. This improved coupling is reflected in less anisotropic superconducting properties (Sect. 50.3). Defects in the BaO/TlO/BaO layers forming the charge-carrier reservoirs provide holes for the doping of the  $\text{CuO}_2$  planes. In the  $\text{Tl-}12(n-1)n$  compounds, the BaO layers can be replaced by SrO layers. The substitution of Tl by Hg leads to the structurally analogous  $\text{Hg-}12(n-1)n$  counterparts. The lattice pa-

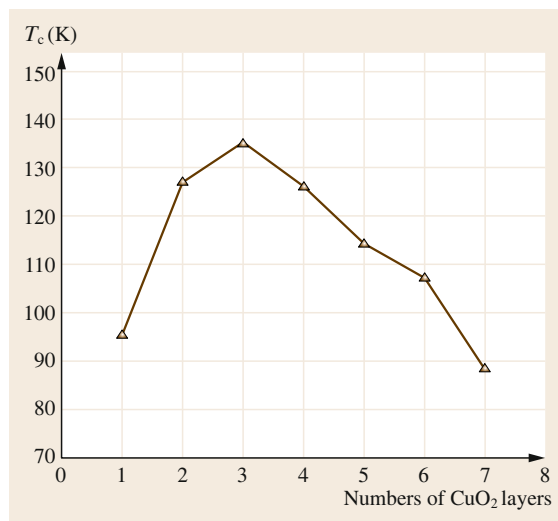


**Fig. 50.21** Critical temperature of  $\text{Hg-}12(n-1)n$  superconductors versus the number  $n$  of  $\text{CuO}_2$  planes in the perovskite (copper oxide) blocks. (After [50.64])

rameters of selected cuprate superconductors are listed in Table 50.4.

#### 50.2.4 Critical Temperatures

Next, some of the factors determining the critical temperature of cuprate superconductors will be discussed. As shown in the generic phase diagram for cuprate superconductors (Fig. 50.15), the critical temperatures of these materials are closely connected to the hole concentration  $p$  in the  $\text{CuO}_2$  planes, which is determined by the formal valence  $2 + p$  of the copper atoms in the conduction planes. Generally, an inverse parabolic dependence of the critical temperature on the number of holes per  $\text{CuO}_2$  has been found. The maximum  $T_c$  is typically reached for a hole concentration  $p$  of 0.15–0.2 holes per  $\text{CuO}_2$ . For hole concentrations above 0.2 holes per  $\text{CuO}_2$  the critical temperature decreases with increasing carrier concentration, leading to a nonsuperconducting metal for  $p > 0.3$  holes per  $\text{CuO}_2$ . As an example of this behavior, the critical temperature of  $\text{HgBa}_2\text{CuO}_{4+\delta}$  as function of the hole concentration is shown in Fig. 50.20.

In addition to the carrier concentration, the number of  $\text{CuO}_2$  planes in the perovskite blocks is of importance for the critical temperature. The maximum critical temperatures of selected cuprate superconductors listed in Table 50.5 clearly indicate that the critical temperature increases with increasing number  $n$  of  $\text{CuO}_2$  planes in the copper oxide blocks, at least up to the compound with  $n = 3$ . For compounds with four or more  $\text{CuO}_2$  planes in the perovskite blocks, the critical tem-

perature decreases with increasing  $n$ . In Fig. 50.21, this behavior is illustrated for the Hg-12 $(n-1)n$  compounds. A possible explanation for the observed behavior is the fact that in cuprates with  $n \geq 3$ , the hole concentrations in the central and outer CuO<sub>2</sub> layers may be considerably different. It may therefore be impossible to reach simultaneously the optimum carrier concentration in all the CuO<sub>2</sub> layers for compounds with  $n \geq 4$ .

Finally, it should be mentioned that the critical temperature of cuprate superconductors has been found to

be connected with the lattice parameters. Consequently, the critical temperature depends on applied pressure. Application of a hydrostatic pressure typically enhances the critical temperature of cuprate superconductors. In Hg-1223, superconductivity was observed at temperatures as high as 164 K at a pressure of 31 GPa [50.65]. A more complex situation results for the application of uniaxial pressure. In the case of pressure along the crystallographic  $a$ - or  $b$ -axis the critical temperature is enhanced, whereas for uniaxial pressure along the  $c$ -direction  $T_c$  is reduced [50.66, 67].

## 50.3 Physical Properties of Cuprate Superconductors

### 50.3.1 Anisotropic Superconductors

As a consequence of the layered crystal structures of the cuprates, the penetration depth depends on the direction of the screening currents. Assuming that the screening currents in the  $a$ - and  $b$ -directions are equal, two different penetration depths  $\lambda_{ab}$  and  $\lambda_c$  result. The indices give the direction of the screening currents. Thus, two different Ginzburg–Landau parameters  $\kappa_{ab}(B||ab)$  and  $\kappa_c(B||c)$  can be defined

$$\begin{aligned}\kappa_{ab} &= \left( \frac{\lambda_{ab}\lambda_c}{\xi_{ab}\xi_c} \right)^{1/2}, \\ \kappa_c &= \frac{\lambda_{ab}}{\xi_{ab}},\end{aligned}\quad (50.20)$$

where  $\xi_{ab}$  and  $\xi_c$  are the coherence lengths in the  $ab$ -plane and along the  $c$ -direction, respectively. The dimensionless anisotropy parameter is given by [50.68]

$$\gamma_a = \left( \frac{m_c}{m_{ab}} \right)^{1/2} = \frac{\lambda_c}{\lambda_{ab}} = \frac{\xi_{ab}}{\xi_c} = \frac{B_{c2,ab}}{B_{c2,c}} = \frac{B_{c1,c}}{B_{c1,ab}},\quad (50.21)$$

where  $m_{ab}$  and  $m_c$  are the effective masses of the charge carriers for in-plane and out-of-plane currents, respectively. The expressions for the upper critical fields are [50.48, 68]

$$\begin{aligned}B_{c2,c} &= \frac{\phi_0}{2\pi\xi_{ab}^2}, \\ B_{c2,ab} &= \frac{\phi_0}{2\pi\xi_c\xi_{ab}}.\end{aligned}\quad (50.22)$$

The upper and lower critical fields of various cuprate superconductors are listed in Table 50.6. The lower critical fields are typically between 10 and 500 mT for

magnetic fields applied along the  $c$ -direction. The upper critical fields of cuprate superconductors can exceed 100 T even for the unfavorable field direction  $B||c$ . The data for Tl-2201, Hg-1201, and Hg, Cu-1201 given in Table 50.6 clearly indicate that the critical fields, like the critical temperatures, depend on the actual doping level.

For the characteristic length scales in cuprate superconductors, the following relation has been found

$$\xi_c < \xi_{ab} \ll \lambda_{ab} < \lambda_c. \quad (50.23)$$

Table 50.7 lists for various cuprate superconductors the penetration depths and the coherence lengths. The in-plane coherence length  $\xi_{ab}$  is typically 1–4 nm. The considerably smaller values found for the out-of-plane coherence length  $\xi_c$  are comparable to interatomic distances. The small values of  $\xi_c$  are responsible for the insulating character of the charge-carrier reservoirs (Fig. 50.14) separating adjacent CuO<sub>2</sub> blocks. The cuprates are therefore nearly two-dimensional superconductors with intrinsic Josephson junctions along the  $c$ -direction. Moreover, the cuprates are extreme type II superconductors with  $\kappa_c$  values around 100.

### 50.3.2 Irreversibility Line

The magnetic phase diagram of cuprate superconductors is much more complicated than that of metallic superconductors. It is beyond the scope of this chapter to describe the details of the magnetic phase diagram of cuprate superconductors. A simplified magnetic phase diagram is shown in Fig. 50.22. An outstanding feature of high-temperature superconductors is the existence of an irreversibility line well below the upper critical field. Above this line, the vortices are movable, and hence the critical current density is zero. The irreversibility line

**Table 50.6** Lower and upper critical fields of various cuprate superconductors

Compound	$B_{c1,c}$ (mT)	$B_{c2,c}$ (T) <sup>a</sup>	Comments	Reference
La, Sr-214		53		[50.69]
La-214		36/50	Ba/Sr doped	[50.70]
Y-123		122	$B_{c2,ab} = 674$ T	[50.71]
Y-123	500	29	$B_{c2,ab} = 140$ T	[50.72]
Y-123	150		$B_{c1,ab} = 24$ mT	[50.73]
Y-123	85		$B_{c1,ab} = 25$ mT	[50.74]
Bi-2201		20.2		[50.75]
Bi-2212		107		[50.76]
Bi-2212		31	$B_{c2,ab} = 476$ T	[50.77]
Bi-2212		71.5	$B_{c2,ab} = 542$ T	[50.78]
Bi, Pb-2212		83/95		[50.79]
Bi-2223		39	$B_{c2,ab} = 1210$ T	[50.80]
Bi, Pb-2223		184		[50.81]
Bi, Pb-2223	13.5			[50.82]
Tl-2201		0.85/1.9	$T_c = 9.7/15.7$ K	[50.83]
Tl-2212		99		[50.76]
Tl-2212	30		$B_{c1,ab} = 0.8$ mT	[50.73]
Tl-2223		75		[50.76]
Tl-1223	37	75		[50.84]
Hg-1201		100		[50.85]
Hg-1201	12.4/8.1		$T_c = 82/87$ K	[50.86]
Hg, Cu-1201		67/160	$T_c = 85/96$ K	[50.87]
Hg-1223		190		[50.42]

<sup>a</sup> Including the upper critical field data of polycrystalline samples

**Table 50.7** Characteristic lengths for selected cuprate superconductors. (Data from [50.39, 42, 85, 87, 88])

Compound	$\lambda_{ab}$ (nm)	$\xi_{ab}$ (nm)	$\xi_c$ (nm)
La, Sr-214	250–410	2.1	
Y-123	130–240	1.3–1.6	0.2–0.3
Bi-2201	438	4.0	
Bi-2212		2.7–3.8	0.16–0.18
Bi-2223		2.9	0.093
Bi, Pb-2212	178	2.0	
Bi, Pb-2223	88–245	1.35–2.9	
Tl-2201		5.2	0.3
Tl-2212		2.0–3.1	0.03–0.68
Tl-2223	117–163	1.1–1.36	
Tl-2234		4.5	1
Tl-1223	137	2.1	
Hg-1201	117–216 <sup>a</sup>	1.7–3.4 <sup>a</sup>	
Hg, Cu-1201	162–283 <sup>a</sup>	1.43–2.2 <sup>a</sup>	
Hg-1223	130–150	1.3	

<sup>a</sup> Different doping levels

can be described by the expression

$$B_{irr} = B_0 \left(1 - \frac{T_{irr}}{T_c}\right)^\alpha, \quad (50.24)$$

where  $B_{irr}$  is the irreversibility field,  $T_{irr}$  is the irreversibility temperature,  $B_0$  is a fitting parameter, and

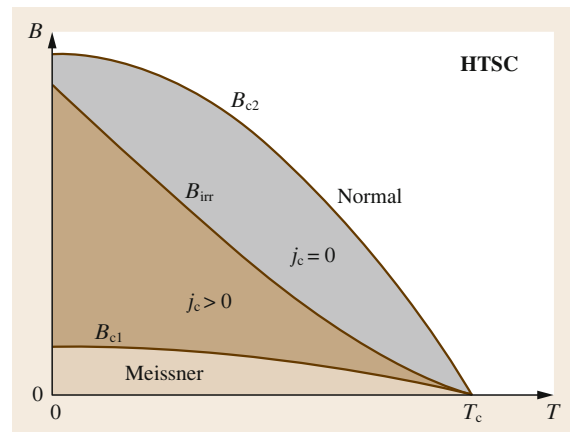


**Fig. 50.22** Simplified magnetic phase diagram of cuprate superconductors. Above the irreversibility line, the vortices are movable, and hence the critical current density is zero. (After [50.39, p. 138])

the exponent  $\alpha$  is characteristic of the superconductor in question. In the case of Y-123, the exponent  $\alpha$  is close to 1.5 for magnetic fields perpendicular to the crystallographic  $c$ -direction, while values around 1.3 have been found for  $B||c$  [50.73].

The existence of the irreversibility line is reflected in the broadening of the resistive transition in the pres-



ence of an applied magnetic field. Figure 50.23 shows the resistive transition of a Bi-2212 single crystal for magnetic fields of 2, 5, and 12 T parallel to the  $c$ -direction. The data for zero applied field are also shown in Fig. 50.23. The end point of the resistive transition corresponds to the irreversibility temperature for the magnetic field applied. On the other hand, the onset of the resistivity drop may be used to determine the upper critical field.

The existence of an irreversibility line can be explained in two different ways. In the more conventional picture, the occurrence of resistance above the irreversibility line is caused by thermally activated depinning. Within this picture, it can be easily understood that the irreversibility line of cuprate superconductors is shifted to higher fields and temperatures by heavy-ion irradiation [50.90–92]. The irradiation generates amorphous tracks, which are efficient pinning centers. An alternative scenario is the melting of the flux-line lattice. Evidence for this possibility is the latent heat measured at the phase transition [50.93, 94].

The maximum operating field of cuprate superconductors is limited by the irreversibility line for the unfavorable field direction  $B||c$ . In any comparison of the behavior of different cuprates the irreversibility field as a function of the reduced temperature  $T/T_c$  should be considered. The highest irreversibility fields result for Y-123, while the lowest values of  $B_{irr}$  have been found for Bi- and Tl-22( $n-1$ ) $n$  compounds. Intermediate irreversibility fields result for Tl- and Hg-12( $n-1$ ) $n$  compounds [50.39, 95]. The observed order in the irreversibility fields indicates that flux pinning is more efficient in cuprates with less anisotropic physical properties. The largest anisotropy of the physical

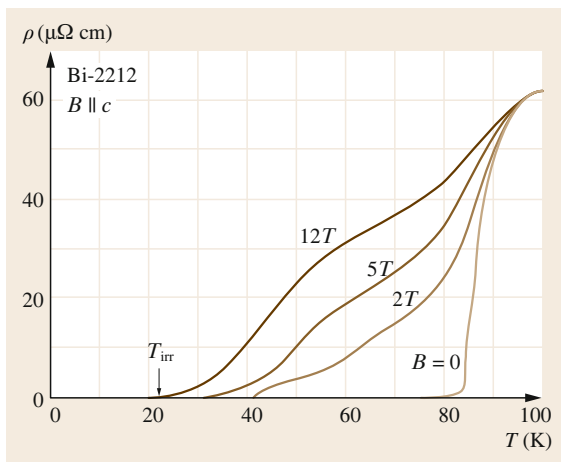


**Fig. 50.23** Resistivity versus temperature curves of a Bi-2212 single crystal for magnetic fields parallel to the  $c$ -direction. (After [50.39, p. 139], results from [50.89])

properties has been observed in Bi- and Tl-22( $n-1$ ) $n$  compounds with the largest distance of adjacent  $\text{CuO}_2$  blocks. The relatively small anisotropy of Y-123 seems to be the consequence of the short-circuiting of the insulating charge-carrier reservoirs by the  $\text{CuO}$  chains (Fig. 50.18).

### 50.3.3 Limitations of the Transport Critical Current

The electric field generated in a superconductor at the transition to the normal conducting state is typically well described by a power law  $E = E_c(I/I_c)^n$ , where  $I$  is the current,  $n$  is the index of resistive transition, and  $E_c$  the electric field used to define the critical current  $I_c$ . Typically  $E_c$  values of 0.1 or  $1 \mu\text{V}/\text{cm}$  are used to determine the critical current.

It should be recognized that, unlike the critical temperature and the upper critical field, the critical current density is not an intrinsic material property. The achievable  $j_c$  values are determined mainly by the microstructure of the superconductor in question. Grain boundaries can act as weak links, leading to small critical current densities in polycrystalline cuprate superconductors. In the absence of grain-boundary weak links, the transport  $j_c$  is mainly determined by flux pinning. Before these effects are discussed, the anisotropy of  $j_c$  in individual grains and epitaxial thin films is considered.

#### Anisotropy of the Critical Current Density

In cuprate superconductors, conductive copper oxide blocks and insulating charge-carrier reservoirs alternate along the crystallographic  $c$ -direction. The currents can easily flow in the conductive  $\text{CuO}_2$  planes, whereas currents along the  $c$ -direction have to cross the insulating or semiconducting charge-carrier reservoirs (tunneling). In spite of  $j_c$  values as high as  $10^8 \text{ A}/\text{cm}^2$  in the  $\text{CuO}_2$  planes of Hg-1212 films, the estimated  $j_c$  along the  $c$ -direction is as low as  $5000 \text{ A}/\text{cm}^2$  [50.96].

A further anisotropy of the critical current density is related to the direction of the applied magnetic field. Figure 50.24 shows the critical current density of an epitaxial Bi-2212 film as a function of the applied magnetic field for selected temperatures. The critical current density declines rapidly with increasing applied field for  $B||c$ , while the field dependence of  $j_c$  is much less pronounced for  $B||ab$ . This behavior reflects the considerably different upper critical fields for these two field directions. The angle dependence of  $j_c$  in epitaxial Bi-2212 and Bi-2223 films can be described by the expression

$$j_c(B, \theta) = j_{c,c}(B \sin \theta), \quad (50.25)$$

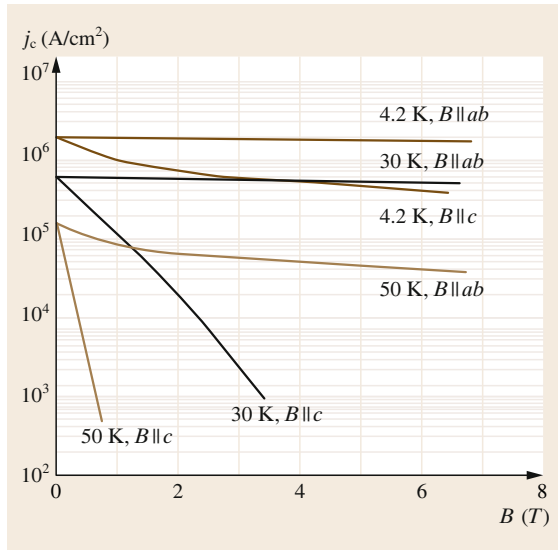


**Fig. 50.24** Critical current densities in epitaxial Bi-2212 films as a function of applied magnetic field for  $B$  along the  $ab$ -planes and parallel to the crystallographic  $c$ -direction. (After [50.97])

where  $\theta$  is the angle between the  $ab$ -planes and the field direction, and  $j_{c,c}$  is the critical current density for  $B||c$ . The above expression states that the reduction of the critical current by an applied magnetic field is determined exclusively by the field component parallel to the  $c$ -direction.

### Grain-Boundary Weak Links

Soon after the discovery of superconductivity above 77 K in Y-123, it was noticed that the transport  $j_c$  in sintered samples is typically well below 1000 A/cm<sup>2</sup>. In addition, magnetic fields of a few mT are sufficient to reduce the  $j_c$  by an order of magnitude. On the other hand, critical current densities well above 10<sup>6</sup> A/cm<sup>2</sup> could be achieved in epitaxial Y-123 films. These experimental results suggest that the grain boundaries present in polycrystalline material can act as barriers for the transport current. Due to extremely short coherence lengths,  $\xi_c < 1$  nm, the Cooper pair density can be considerably reduced within the width of a grain boundary. Two grains separated by a grain boundary can therefore be considered as a Josephson junction.

The high  $j_c$  values achieved in highly textured films suggest that low-angle grain boundaries are strongly coupled. To clarify this aspect, the transport properties of artificial grain boundaries have been studied [50.98, 99]. In epitaxial growth the crystallography prescribed by the substrate can be transmitted to the Y-123 film. Using SrTiO<sub>3</sub> bicrystals, two Y-123 grains connected by an artificial grain boundary with a well-defined mis-

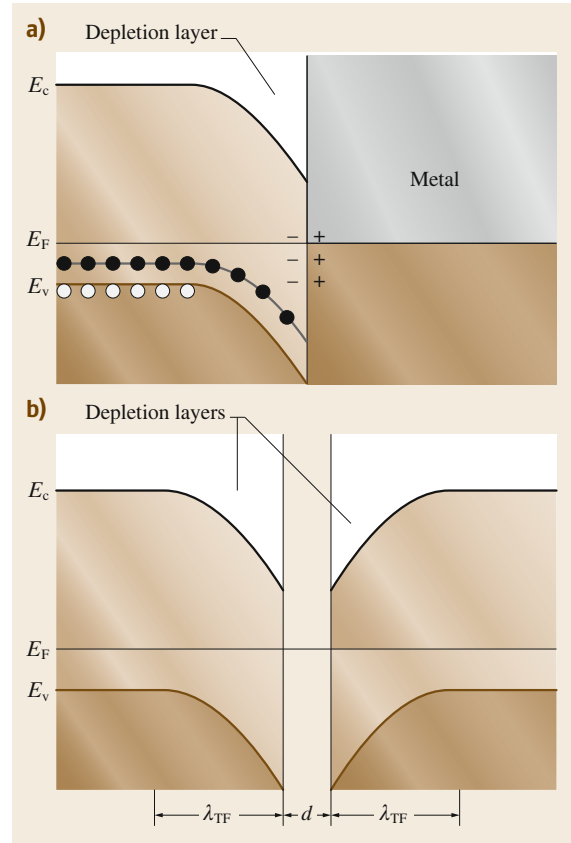


**Fig. 50.25a,b** Space-charge effects and band bending at a semiconductor–metal interface (a) and at a grain boundary in a cuprate superconductor (b). (After [50.102])

orientation angle  $\theta$  can be prepared. The critical current density across the grain boundaries has been found to decrease rapidly with increasing misalignment angle. For [001]-tilt boundaries (rotation of the second grain around the common  $c$ -axis) in Y-123 films, the grain boundary  $j_c$  depends exponentially on the misalignment angle  $\theta$

$$j_c = j_{c0} \exp\left(-\frac{\theta}{\theta_0}\right), \quad (50.26)$$

where  $\theta_0 \cong 6.3^\circ$  and  $j_{c0} \cong 2 \times 10^7$  A/cm<sup>2</sup> at 4.2 K [50.100]. The corresponding values for Bi-2223 [001]-tilt grain boundaries are  $j_{c0} = 6 \times 10^6$  A/cm<sup>2</sup> and  $\theta_0 = 5^\circ$  at 26 K [50.101].

The weak-link behavior is closely related to the strong reduction of the Cooper pair density in the grain boundaries caused by the extremely short coherence lengths and the low carrier concentrations in cuprate superconductors. The carrier concentration in optimally doped cuprate superconductors is around  $5 \times 10^{21}$  cm<sup>-3</sup>,

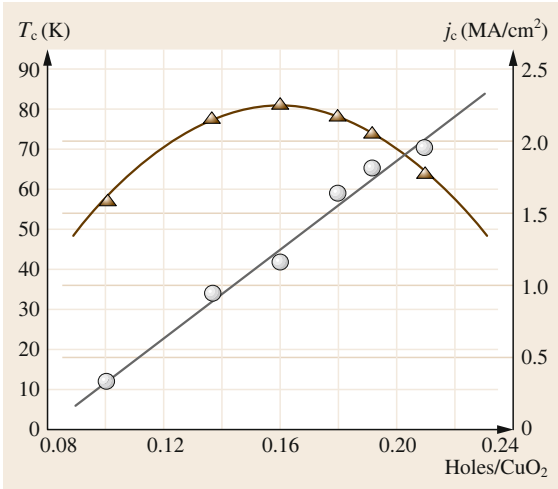


**Fig. 50.26** Critical temperature (triangles) and current density (circles) of a symmetric 24° [001]-tilt boundary as a function of the hole concentration. The charge-carrier concentration in the bicrystalline  $\text{Y}_{0.7}\text{Ca}_{0.3}\text{Ba}_2\text{Cu}_3\text{O}_{7-\delta}$  films has been modified by annealing at different oxygen pressures. (After [50.100])

whereas the carrier concentration in copper is as high as  $85 \times 10^{21} \text{ cm}^{-3}$ . Furthermore, the behavior of grain boundaries in cuprate superconductors is similar to that of semiconductor–metal interfaces [50.102, 103]. In the case of a p-type semiconductor in contact with a metal characterized by a smaller work function, electrons flow from the metal into the semiconductor. As a consequence, both the valence and the conduction band are bent downward (Fig. 50.25a). There an excess of negatively charged acceptor ions and a depletion of holes in the valence band result. Currents from the metal to the semiconductor would further enlarge the space-charge region and are therefore negligible (Schottky contact). Because of low carrier concentrations and large dielectric constants ( $\epsilon \approx 10$ ), band-bending effects can occur in cuprate superconductors. The grain boundaries of cuprate superconductors may be considered as double Schottky barriers (Fig. 50.25b). The resulting Thomas–Fermi screening length is in the range of 0.5–1 nm, which is comparable to the coherence length. The width of the insulating layer at the grain boundary is  $t = d + 2l_d$ , where  $d$  is the structural width of the boundary and  $l_d$  the thickness of the depletion layer. The structural width of typical grain boundaries is  $\approx 0.4$  nm. On the other hand, the thickness of the depletion layer is 0.16 nm for  $\epsilon = 10$ , an in-built voltage of 0.1 V, and a carrier concentration of  $4.5 \times 10^{21} \text{ cm}^{-3}$  [50.102]. Consequently, the total thickness of the insulating layer is considerably enhanced by the space-charge region.

In such a scenario it should be possible to modify the electronic properties of the interface by increasing the carrier concentration. In Y-123 this can be done by Ca doping. Figure 50.26 shows for symmetric 24° [001]-tilt boundaries the critical temperature and current density as a function of the hole concentration. As expected the  $j_c$  values at 4.2 K increase with increasing hole concentration even in the over-doped region, where  $T_c$  decreases.

### Flux Pinning

Transport currents without losses can only flow in a type II superconductor when the flux lines are effectively pinned. The screening currents circulating around each flux line are responsible for a repulsive vortex–vortex interaction, which prevents flux motion as soon as a sufficiently large fraction of the flux lines is pinned. The effectiveness of this collective pinning depends on the stiffness of the flux-line lattice.

The energy required to create a flux line can be estimated from the lower critical field  $B_{c1}$  [50.47]. At the lower critical field, flux lines start to enter the superconductor. The formation energy for each flux line is therefore

$$E_{fl} = \int_0^{B_{c1}} m dB \quad \text{with} \quad m = \frac{\phi_0}{\mu_0} l_{fl}, \quad (50.27)$$

where  $m$  is the magnetic moment of a flux line of length  $l_{fl}$  containing a single flux quantum. The required energy per unit length is

$$\frac{E_{fl}}{l_{fl}} = \frac{\phi_0}{\mu_0} B_{c1}. \quad (50.28)$$

Using  $\kappa = \lambda_L/\xi$  the lower critical field can be written as [50.42]

$$B_{c1} = \frac{\phi_0 \ln \kappa}{4\pi\lambda_L^2}. \quad (50.29)$$

When the flux line is in a normal region, no energy is required to form the normal vortex core, and the resulting pinning energy per unit length is

$$\frac{E_{fl}}{l_{fl}} = \frac{1}{4\pi\mu_0} \left( \frac{\phi_0}{\lambda_L} \right)^2 \ln \left( \frac{\lambda_L}{\xi} \right). \quad (50.30)$$

Generally, regions with reduced Cooper pair densities due to defects can act as pinning centers.

The pinning properties of the cuprate superconductors are highly anisotropic. Relatively strong pinning has been found for magnetic fields transverse to the current direction applied in the  $ab$  plane. For the resulting

Lorentz force along the  $c$ -direction, strong intrinsic pinning may be provided by the insulating charge-carrier reservoirs of the layered structure along the  $c$ -direction. On the other hand, the pinning is weak for magnetic fields transverse to the current direction applied along the  $c$ -direction, leading to a Lorentz force parallel to the  $ab$ -planes. Flux lines along the  $c$ -direction experience strong pinning only within the  $\text{CuO}_2$  blocks. As a consequence of the layered structure, the vortices may be cut into vortex segments or even pancake vortices

which exist only within the conductive  $\text{CuO}_2$  blocks. These pancake vortices could easily move in the direction of the Lorentz force.

The positions of the irreversibility lines in the different cuprate superconductors reflect the anisotropy of the pinning properties. Typically, the pinning efficiency for magnetic fields along the  $c$ -direction decreases as one progresses from Y-123 via the Hg- and Tl- $12(n-1)n$  compounds to the highly anisotropic Bi- and Tl- $22(n-1)n$  cuprates.

## 50.4 Superconducting Films

Because of the weakly coupled large-angle grain boundaries present in polycrystalline bulk material, the transport critical current density is much smaller than the  $j_c$  of the individual grains. In contrast to polycrystalline bulk material, adjacent grains of epitaxial films are connected by low-angle grain boundaries. As a consequence, the critical current densities measured in epitaxial films are close to the  $j_c$  values of individual grains. At low temperatures and zero applied field, the critical current densities in epitaxial Y-123, Bi-2212, Bi-2223 and Hg-1223 films exceed  $10^7 \text{ A/cm}^2$  [50.97, 104–106]. Even at 77 K,  $j_c$ -values well above  $10^7 \text{ A/cm}^2$  have been measured in Y-123 films [50.107].

The physical properties of ultrathin films can be considerably different from those of bulk single crystals. First, let us consider the effect of the film thickness on the critical temperature. For the growth of epitaxial ultrathin films, a substrate with good lattice matching is required.  $\text{YBa}_2\text{Cu}_3\text{O}_7$  films of thickness equal to the height of a single unit cell in the  $c$ -direction can be grown onto  $\text{SrTiO}_3$  single crystals covered by a six-unit-cell-thick nonsuperconducting  $\text{PrBa}_2\text{Cu}_3\text{O}_7$  (Pr-123) buffer layer [50.108]. The lattice mismatch of Y-123 and Pr-123 is less than 1.5%. The layer growth can be checked by the observation of the strong intensity oscillations of reflection high-energy electron diffraction. The period of these oscillations has been found to correspond to the height of a single unit cell. Y-123 films with a thickness of 1–10 unit cell heights were grown by coevaporation of the metals under oxygen atmosphere. To provide hole doping the ultrathin Y-123 films are covered by a six-unit-cell-thick Pr-123 layer. The offset critical temperature of these Y-123 films is considerably lower than that of a 100-nm-thick film (Fig. 50.27). On the other hand, the onset critical temperature has been found to be much less affected. The reduction of the offset critical temperature has been attributed to the more pronounced critical fluctuations in the thinner films.

Critical fluctuations are variations of the superconducting order parameter  $\psi = n_c^{1/2} \exp(i\varphi)$  ( $n_c$  is the Cooper pair density) around the thermal equilibrium values.

The critical temperature of ultrathin Y-123 layers in Y-123/Pr-123 multilayers has been found to depend on the thicknesses of the insulating Pr-123 layers [50.109]. The thickness of 1.2 nm of the embedded Y-123 layers corresponds to the height of a single unit cell in the  $c$ -direction. The critical temperature of the Y-123/Pr-123 multilayer decreases from  $\approx 50 \text{ K}$  (10% of normal-state resistance) to  $\approx 13 \text{ K}$  for Pr-123 interlayer thicknesses of 1.2 and 7.2 nm, respectively. Because of the Josephson coupling of adjacent Y-123 layers in the multilayer the critical fluctuations are expected to be less pronounced than in a single Y-123 film

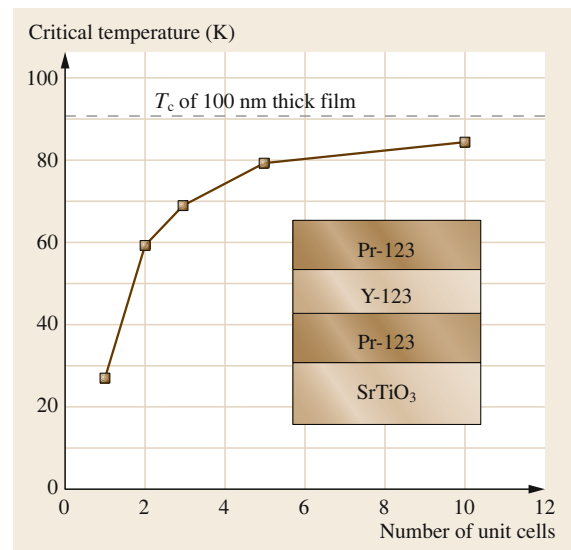


**Fig. 50.27** Offset critical temperature of ultrathin Y-123 films as a function of the layer thickness normalized to the  $c$  lattice parameter. (After [50.108])

of the same thickness. Thus, the  $T_c$  of the Y-123 layers in the Y-123/Pr-123 multilayer with a Pr-123 thickness of 1.2 nm is higher than that of a single Y-123 layer of the same thickness (Fig. 50.27).

Finally, let us consider the effects of epitaxial strain on the critical temperature of (La, Sr)<sub>2</sub>CuO<sub>4</sub> films [50.67, 110, 111]. In epitaxial growth, the crystallography prescribed by the substrate is transmitted to the film. For a sufficiently small film thickness, the lattice constant of the film is equal to that of the substrate. As a consequence of the lattice mismatch a considerable epitaxial strain can be induced in the film. Under epitaxial growth conditions, a compressive strain in the CuO<sub>2</sub> planes of (La, Sr)<sub>2</sub>CuO<sub>4</sub> is accompanied by a tensile strain in the  $c$ -direction. Typically, in-plane compressive and out-of-plane tensile strains enhance the  $T_c$  of cuprate superconductors. Thus, the critical temperature of cuprate superconductors should be much more sensitive to epitaxial strain effects than to hydrostatic pressure, where the opposite in-plane and out-of-plane effects partly cancel each other. Because of film deposition at temperatures above 750 °C, differences in the thermal expansion coefficients provide an additional contribution to the strain in the films. In thick films the epitaxial strain is released by the appearance of misfit dislocations. The expected change in the critical temperature of the films is given by

$$T_c = T_c(0) + 2 \frac{dT_c}{d\varepsilon_{ab}} \varepsilon_{ab} + \frac{dT_c}{d\varepsilon_c} \varepsilon_c, \quad (50.31)$$

where  $\varepsilon = (d_{\text{bulk}} - d_{\text{strained}})/d_{\text{bulk}}$ , with  $d$  being a lattice parameter.

To study the epitaxial strain effects, *Locquet* et al. [50.67] deposited La<sub>1.9</sub>Sr<sub>0.1</sub>CuO<sub>4</sub> films ( $a = 0.3784$  nm,  $\alpha = 8.5 \times 10^{-6}$  K<sup>-1</sup>) of 10–15 nm thickness on SrTiO<sub>3</sub> ( $a = 0.3905$  nm,  $\alpha = 9 \times 10^{-6}$  K<sup>-1</sup>) and SrLaAlO<sub>4</sub> ( $a = 0.3754$  nm,  $\alpha = 10.5 \times 10^{-6}$  K<sup>-1</sup>) sub-

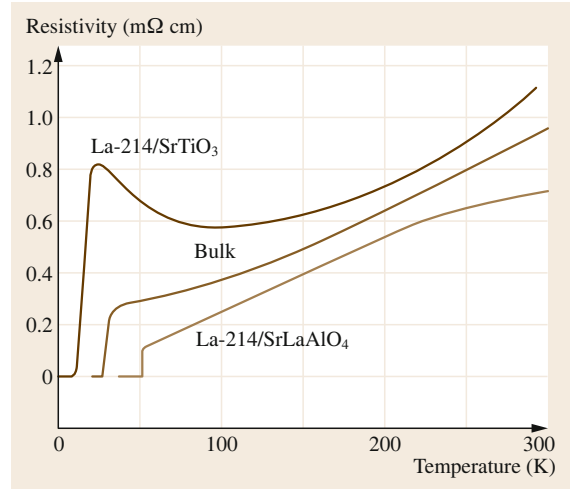


**Fig. 50.28** Resistivity versus temperature for La-214 films on SrTiO<sub>3</sub> and SrLaAlO<sub>4</sub> substrates. The different epitaxial strains lead to considerably different critical temperatures of 10 and 49 K. For comparison the resistivity of La-214 bulk material ( $T_c = 25$  K) is also shown. (After [50.67])

strates. Using x-ray diffraction, strain values of  $\varepsilon_{ab} = 0.63\%$  and  $\varepsilon_c = -0.76\%$  have been determined for the La-214 film on SrTiO<sub>3</sub>. The corresponding strain values for the La-214 film deposited onto SrLaAlO<sub>4</sub> are  $\varepsilon_{ab} = -0.54\%$  and  $\varepsilon_c = 0.35\%$ . The results of *Locquet* et al. [50.67] are shown in Fig. 50.28. The critical temperatures of the La-214 films of 10 (SrTiO<sub>3</sub>) and 49 K (SrLaAlO<sub>4</sub>) are, as expected, considerably different from the bulk value of 25 K. In addition, the temperature dependencies of the normal state resistivities of the two films are remarkably different. The film experiencing a tensile in-plane strain shows an upturn of the normal state resistance at temperatures below 100 K, which is an effect also found in under-doped cuprate superconductors.

## 50.5 The Special Case of MgB<sub>2</sub>

In spite of the fact that MgB<sub>2</sub> has been known since the early 1950s, it was unknown until 2001 that it is a superconductor with a remarkably high transition temperature. Figure 50.29 shows the hexagonal crystal structure of MgB<sub>2</sub>, consisting of alternating layers of boron and magnesium. As a consequence of the layered structure, anisotropic physical properties result. The arrangement of the boron atoms is the same as that of the carbon atoms in graphite. Each of the boron atoms is surrounded by three other boron atoms at the same distance.

To study the role of phonons in the superconductivity of MgB<sub>2</sub>, the critical temperatures of isotopically pure Mg<sup>10</sup>B<sub>2</sub> and Mg<sup>11</sup>B<sub>2</sub> specimens have been studied [50.117]. The transition temperatures of Mg<sup>11</sup>B<sub>2</sub> and Mg<sup>10</sup>B<sub>2</sub> defined by a 2% onset criterion are 39.2 and 40.2 K, respectively. Defining a partial boron isotope-effect exponent  $\beta_B = \Delta \ln T_c / \Delta \ln M_B$ , where  $M_B$  is the atomic mass of boron, a value of  $\beta_B = 0.26 \pm 0.03$  results from the experimental data. On the other hand, the isotope effect for <sup>26</sup>MgB<sub>2</sub> and <sup>24</sup>MgB<sub>2</sub> is much less pronounced [50.118]. The shift of

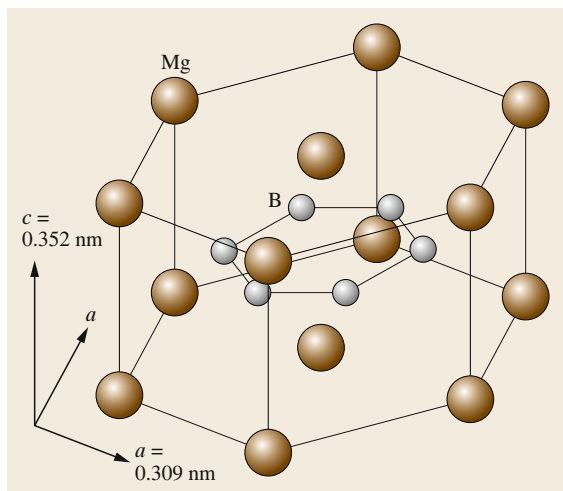


**Fig. 50.29** Hexagonal crystal structure of MgB<sub>2</sub> consisting of alternating layers of magnesium and boron. (After [50.15])

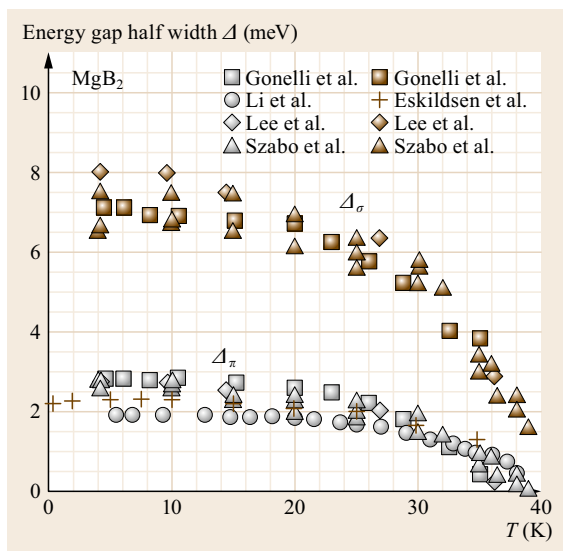


**Fig. 50.30** Half-widths of the  $\sigma$ - and  $\pi$ -band gaps of MgB<sub>2</sub>. (After [50.112–116])

0.1 K in  $T_c$  corresponds to a partial Mg isotope-effect exponent  $\beta_{\text{Mg}}$  of 0.02. The strong boron isotope effect suggests that the pairing of the electrons is caused by the boron phonons. Thus, MgB<sub>2</sub> seems to be a conventional metallic superconductor with an extremely high transition temperature. The high transition temperature seems to be caused by the small atomic mass of boron, leading to high phonon frequencies.

The currently known physical properties of MgB<sub>2</sub> are summarized in Table 50.8. As in cuprate super-

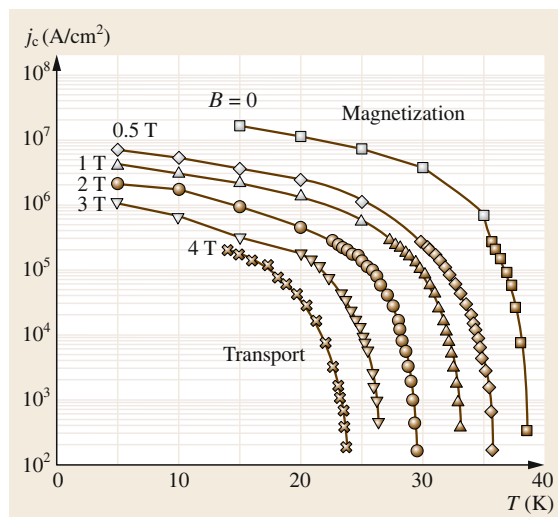


**Fig. 50.31** Critical current density of a  $c$ -axis-oriented MgB<sub>2</sub> film as a function of temperature for magnetic fields up to 4 T. (After [50.133])

conductors, the operation range of MgB<sub>2</sub> is limited by the irreversibility field. In polycrystalline bulk samples, the irreversibility field typically reaches 50% of  $B_{c2}$ . In nanocrystalline MgB<sub>2</sub> bulk material the irreversibility field is shifted to 80% of  $B_{c2}$ . The enhancement of the irreversibility field in the nanocrystalline material has been attributed to the improved pinning provided by the large number of grain boundaries [50.119]. Maximum irreversibility fields of more than 14 T at 4.2 K have been reported for MgB<sub>2</sub> bulk material annealed in Mg vapor [50.120]. MgB<sub>2</sub> is an extreme type II superconductor with a Ginzburg–Landau parameter  $\kappa$  of 38. The coherence length of  $\xi_c \approx 2.5 \text{ nm}$  is considerably larger than the values of  $\approx 0.2 \text{ nm}$  measured for cuprate superconductors (Table 50.7). The anisotropy of the upper critical fields reported for  $c$ -axis-oriented films [50.121] and single crystals [50.122] is typically close to  $B_{c2,ab}/B_{c2,c} \approx 3$ .

A special feature of MgB<sub>2</sub> is the existence of two energy gaps. In MgB<sub>2</sub>, layers of Mg<sup>2+</sup> ions and metallic boron alternate along the crystallographic  $c$  direction (Fig. 50.29). The electronic structure of MgB<sub>2</sub> is similar to that of graphite. The highest occupied electronic states are  $\sigma$ - and  $\pi$ -bonding boron orbitals [50.134–136]. The incompletely filled  $\sigma$ -bands are confined to the boron planes, while the nonbonding  $\pi$ -electrons fill two three-dimensional metallic bands. Band structure calculations indicate that  $\sigma$ -electrons are transferred to the  $\pi$ -bands [50.134]. The superconductivity of MgB<sub>2</sub> is dominated by the  $\sigma$ -band holes, which are strongly coupled to the in-plane vibrations of boron atoms,

**Table 50.8** Physical properties of MgB<sub>2</sub>

Parameter	Value	Comments	Reference
$T_c$ (K)	40.2	Mg <sup>10</sup> B <sub>2</sub>	[50.117]
Lattice parameters		Crystal structure	[50.15]
$a$ (nm)	0.3086	Hexagonal	
$c$ (nm)	0.3524	Space group P6/mmm	
$\rho$ (m $\Omega$ cm)	1–18	at 40 K	[50.120]
$\rho$ (300 K)/ $\rho$ (40 K)	15–3		[50.120]
$B_{c1}$ (mT)	18–26.5	$T = 0$	[50.123, 124]
$B_{c1,ab}$ (mT)	22	Single crystal, $T = 0$	[50.125]
$B_{c1,c}$ (mT)	63	Single crystal, $T = 0$	[50.125]
$B_{c2,ab}$ (T)	19.6/26.4	Films $T_c$ : 37.5/31.4 K, $T = 0$	[50.126]
$B_{c2,c}$ (T)	13.8/14.6	Films $T_c$ : 37.5/31.4 K, $T = 0$	[50.126]
$B_{c2,ab}$ (T)	14.5	Single crystal, $T = 0$	[50.125]
$B_{c2,c}$ (T)	3.18	Single crystal, $T = 0$	[50.125]
$B_{irr}$ (T)	> 14/ $\approx$ 6	$T = 4.2/20$ K	[50.120]
$B_{irr}$ (T)	14.5–25.5	Tapes	[50.127, 128]
$\xi_{ab}$ (nm)	6.8–8.1	$T = 0$	[50.124, 129]
$\xi_c$ (nm)	2.3–2.7	$T = 0$	[50.124, 129]
$\lambda$ (nm)	110–180	$T = 0$	[50.123, 130]
$\lambda_{ab}$ (nm)	82	Single crystal, $T = 0$	[50.125]
$\lambda_c$ (nm)	370	Single crystal, $T = 0$	[50.125]
$\kappa = \lambda/\xi$	38	Polycrystalline, $T = 0$	[50.123]
$\kappa_{ab} = (\lambda_{ab}\lambda_c/\xi_{ab}\xi_c)^{0.5}$	37.1	Single crystal, $T = 0$	[50.125]
$\kappa_c = \lambda_{ab}/\xi_{ab}$	8.1	Single crystal, $T = 0$	[50.125]
$\Delta$ (meV)	8.5–9.5 <sup>a</sup>	$T = 4.2$ K	[50.131]
$\Delta_\sigma$ (meV)	6.5–8		[50.112–116]
$\Delta_\pi$ (meV)	1.9–2.8		[50.113, 115, 116]

<sup>a</sup> MgB<sub>2</sub> is a double gap superconductor (see for example [50.132])

leading to strong pairing and an energy gap with half-width  $\Delta_\sigma \approx 7$  meV [50.135]. In addition, weaker pairs ( $\Delta_\pi \approx 2$  meV) are formed by the  $\pi$ -electrons [50.135]. The measured values of the half-widths of the two energy gaps are presented in Fig. 50.30.

Immediately after the discovery of superconductivity in MgB<sub>2</sub>, the current transport across grain boundaries was studied [50.137, 138]. The results of these investigations indicate that the grain boundaries in MgB<sub>2</sub> do not act as weak links. This behavior reflects the fact that the coherence length of MgB<sub>2</sub> is considerably larger than that of cuprate superconductors.

To give an impression of the current-carrying capacity of MgB<sub>2</sub>, the critical current density of  $c$ -axis-oriented films as a function of temperature is shown in Fig. 50.31 for selected applied magnetic fields ( $B||c$ ). The critical current density at 15 K and zero applied field is as high as 16 MA/cm<sup>2</sup> [50.133, 139], which is comparable to the  $j_c$  values of cuprate superconductors.

Finally, let us briefly consider the synthesis of MgB<sub>2</sub>. Polycrystalline MgB<sub>2</sub> can be synthesized by the reaction of boron powder with magnesium vapor. Stoichiometric quantities of boron and magnesium are sealed into a tantalum tube under an argon atmosphere. In addition, the tantalum tube containing the B/Mg mixture is sealed into a quartz ampoule. To form the desired MgB<sub>2</sub> intermetallic compound, the mixture is heat treated at 950 °C for 2 h [50.140]. In a similar way boron precursor films can be converted to MgB<sub>2</sub> in the presence of Mg vapor. The annealing temperature for the formation of MgB<sub>2</sub> films is typically in the 850 °C range. Very recently  $c$ -axis-oriented epitaxial MgB<sub>2</sub> films were grown onto Al<sub>2</sub>O<sub>3</sub> substrates [50.121]. For applications in electronics, it is desirable to grow the MgB<sub>2</sub> films in situ in a single step on a suitable substrate. The substrate and electronic materials ZrO<sub>2</sub>, MgO, TiN, TaN, AlN, and SiC show no reaction with MgB<sub>2</sub> up to an annealing temperature of 800 °C [50.141].

## 50.6 Iron-Based Superconductors

In 2008, *Hosono* and collaborators discovered that  $\text{LaO}_{1-x}\text{F}_x\text{FeAs}$  is a superconductor with a critical temperature of 26 K [50.16]. Very recently a critical temperature, as high as 58.1 K, was reported for  $\text{SmO}_{0.74}\text{F}_{0.26}\text{FeAs}$  [50.142]. Because of these high critical temperatures, the iron-based superconductors are considered as a second class of complex high-temperature superconductors. There exist four main families of iron-based superconductors, which, like the cuprates, are characterized by layered crystal structures. The (1111)-family can be represented by the chemical formula  $\text{REOFeAs}$ , where RE is a rare earth element. Layers of REO and FeAs alternate along the crystallographic  $c$  direction. Figure 50.32 shows a sketch of the tetragonal crystal structure of the undoped  $\text{LaOFeAs}$  (La-1111) at room temperature.

In a second family of iron-pnictide superconductors, layers of earth alkaline ions alternate with  $\text{Fe}_2\text{As}_2$  layers. These (122) compounds crystallize with a tetragonal crystal structure (space group  $I4/mmm$ ) [50.145,

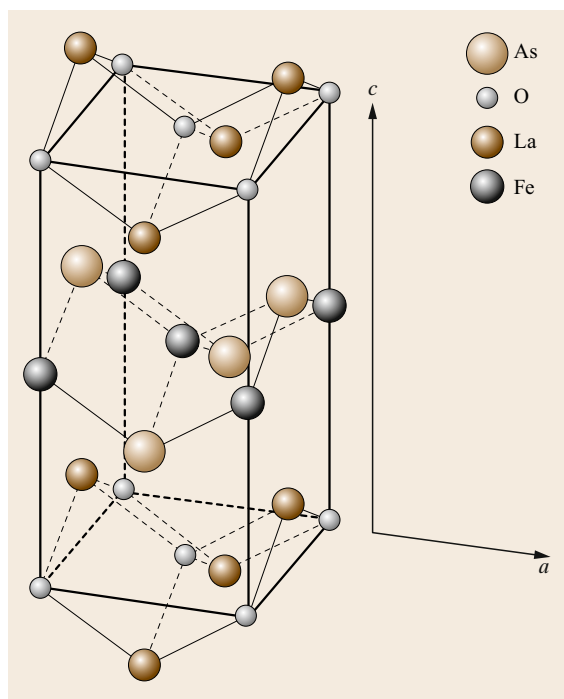


**Fig. 50.32** Sketch of the tetragonal crystal structure of  $\text{LaOFeAs}$  (space group  $P4/nmm$ ). The lattice parameters of the non-fluorine-doped compound are  $a = 0.4033$  nm and  $c = 0.8741$  nm [50.143]. The  $z$  positions of the atoms are  $z = 0$  and  $z = c$  for oxygen,  $z = 0.141c$  and  $z = 0.859c$  for La,  $z = 0.5c$  for Fe and  $z = 0.348c$  and  $z = 0.652c$  for As [50.143]. (After [50.144, 145])

146]. Figure 50.33 shows as an example the tetragonal crystal structure of  $\text{CaFe}_2\text{As}_2$  (Ca-122) [50.146].

In the (111)-family of iron-pnictide superconductors, FeAs layers alternate with layers of alkali ions (Li, Na) along the crystallographic  $c$  direction [50.147, 148].

In the cuprate superconductors, the current flows mainly along the conductive  $\text{CuO}_2$  planes, which are separated by the insulating layers of the charge-carrier reservoirs (Fig. 50.14). The iron-pnictide superconductors are characterized by layered crystal structures similar to the cuprates. In the iron pnictides, the FeAs layers are conductive, while the layers of REO ((1111)-family), alkaline earth ions ((122)-family) and alkali ions ((111)-family) act as charge-carrier reservoirs. A further analogy to the cuprate superconductors is the fact that the nondoped parent compounds are not superconducting. However, the parent compounds of the iron-pnictide superconductors are metals showing an antiferromagnetic order, whereas the parent compounds of the cuprate superconductors are antiferromagnetic Mott insulators. Doping suppresses the antiferromagnetic ordering and the low-temperature

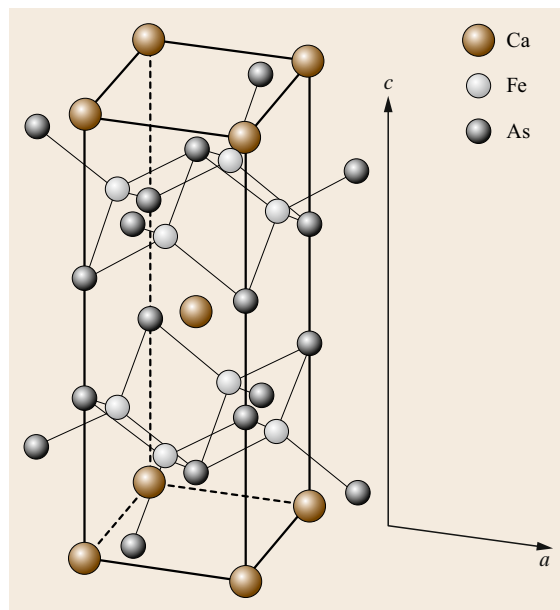


**Fig. 50.33** Sketch of the tetragonal crystal structure of  $\text{CaFe}_2\text{As}_2$  (space group  $I4/mmm$ ). The lattice parameters of the nondoped compound are  $a = 0.3872$  nm and  $c = 1.1730$  nm at room temperature [50.146]. The  $z$  positions of the atoms are  $z = 0$ ,  $z = 0.5c$  and  $z = c$  for Ca,  $z = 0.25c$  and  $z = 0.75c$  for Fe, and  $z = 0.133c$ ,  $z = 0.367c$ ,  $0.633c$  and  $z = 0.867c$  for As. (After [50.145, 146])



transition from a tetragonal to an orthorhombic crystal structure (Fig. 50.34).

The critical temperature of iron-pnictide superconductors depends on the doping level. In LaOFeAs, superconductivity can be established by fluorine doping. The charges per formula unit of LaOFeAs are +1 in the LaO layer and -1 in the FeAs layer. The charges of La, O, and F are +3, -2 and -1 respectively. Substitution of 10% of the oxygen atoms by fluorine (leading to LaO<sub>0.9</sub>F<sub>0.1</sub>FeAs) increases the charge of the LaO layer to +1.1. For charge neutrality, the negative charge of the FeAs layer must be increased to -1.1, i. e., the FeAs layer is doped with electrons. In a similar way, replacement of Ba by K leads to hole doping in Ba<sub>1-x</sub>K<sub>x</sub>Fe<sub>2</sub>As<sub>2</sub>.

In contrast to cuprate superconductors, in which doping in the CuO<sub>2</sub> planes is detrimental for superconductivity, cobalt doping for iron can establish superconductivity in Ba(Fe, Co)<sub>2</sub>As<sub>2</sub> [50.148]. Furthermore, phosphorous doping leads to superconductivity

in BaFe<sub>2</sub>(As, P)<sub>2</sub> without the introduction of additional charge carriers to the FeAs planes [50.150]. In the iron-pnictide superconductors, not only the addition of charge carriers but also the effect of doping on the crystal structure are of importance.

In addition to the iron pnictides, there exists a fourth family of iron-based superconductors without FeAs layers. In this (11)-family with the chemical formula FeCh, where Ch represents Se, Te, or S, the FeAs layers are replaced by iron chalcogenide layers. Moreover, there are no layers to act as charge-carrier reservoirs [50.148].

The next aspect to be considered are the phase diagrams of LaO<sub>1-x</sub>F<sub>x</sub>FeAs (La-1111) [50.148] and Ba<sub>1-y</sub>K<sub>y</sub>Fe<sub>2</sub>As<sub>2</sub> (Ba-122) [50.149] (Fig. 50.34). The La-1111 parent compound without fluorine doping shows a transition from a tetragonal to an orthorhombic structure at a temperature  $T_s \approx 155$  K. Slightly below 140 K, antiferromagnetic ordering has been observed. Doping with fluorine suppresses both the structural instability and the antiferromagnetic order. Above 4.5% fluorine doping, superconductivity is observed, and a maximum critical temperature of 26 K is reached at around 10%. In the case of the Ba-122, the establishment of an antiferromagnetic spin density wave (SDW) order is accompanied by a structural change from a tetragonal to an orthorhombic structure. In the nondoped parent compound, the transition to the orthorhombic crystal structure and the SDW order occurs around 140 K. Doping suppresses the structural instability and the antiferromagnetic SDW order. Superconductivity can exist above 10% potassium doping. For doping levels between 10 and 25% superconductivity and SDW order can coexist in Ba-122 in the orthorhombic crystal structure. The maximum critical temperature of around 38 K is reached when around 40% of the barium atoms are replaced by potassium.

The known physical properties of various iron-based superconductors are listed in Table 50.9. The maximum critical temperatures of (1111) compounds exceed 50 K. For Ba-122 and Sr-122, maximum critical temperatures of 38 K have been reported. The (1111) compounds crystallize in a tetragonal crystal structure with the space group P4/nmm. The lattice parameters of the fluorine-doped compounds are slightly shorter than those of the parent compounds. For the compounds considered, the *a* lattice parameters are in the range of 0.3932 and 0.4039 nm, while the *c* lattice parameters are between 0.8490 and 0.8742 nm. The crystal structures of the (122) compounds are body-centered tetragonal (space group I4/mmm). The lattice parameters of the nondoped Ba-122 are *a* = 0.3964 nm and *c* = 1.3022 nm. In some of the iron-pnictide superconductors, evidence for the existence of two gaps has been found. The ratio of  $2\Delta/T_c$  is between 3 and 4

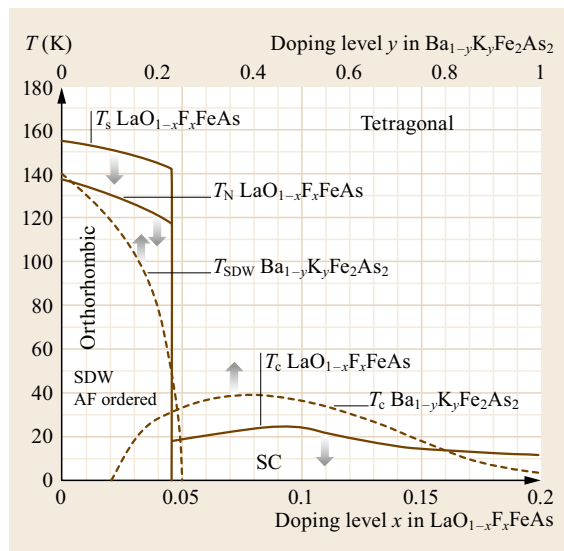


**Fig. 50.34** Phase diagrams of La-1111 (solid lines) [50.148] and Ba-122 (dotted lines) [50.149]. In the case of La-1111, the  $T_s$  line indicates the temperature of the structural transformation from a tetragonal to an orthorhombic structure. At a slightly lower temperature  $T_N$ , a transition to an antiferromagnetic state occurs. Above 4.5% fluorine doping, superconductivity is observed, while the transition to an orthorhombic crystal structure and antiferromagnetic ordering is suppressed. For Ba-122, the transition to an orthorhombic crystal structure and SDW ordering occurs at the same temperature  $T_{SDW}$ . Again, doping suppresses of the structural transition and the antiferromagnetic SDW ordering. A maximum critical temperature of  $\approx 38$  K is reached for  $y = 0.4$

for the smaller gap, and above 7 for the larger. A characteristic feature of the iron-based superconductors is an extremely high upper critical field of the order of 100 T. Because of the layered crystal structures, the physical properties of iron-based superconductors are anisotropic. The coherence length along the FeAs (*ab*) planes varies between 1.2 and 5 nm, while along the *c* direction it is in the range of 0.35 to 1.2 nm. The penetration depth for screening currents flowing in the *ab* planes is of the order of 200 nm.

The last aspect to be considered is the critical current density in iron-based superconducting films. The critical current densities of Fe(Te,Se) [50.177], Ba(Fe, Co)<sub>2</sub>As<sub>2</sub> [50.178], BaFe<sub>2</sub>(As, P)<sub>2</sub> [50.179], and IBAD-MgO/Ba(Fe, Co)<sub>2</sub>As<sub>2</sub> films [50.180] are presented in Fig. 50.35. The critical current densities at 4.2 K and zero applied field reach values between 0.4 (Fe(Te,Se)) and 3.5 MA/cm<sup>2</sup> (BaFe<sub>2</sub>(As, P)<sub>2</sub>). For the Ba(Fe, Co)<sub>2</sub>As<sub>2</sub> film, critical current densities for fields applied parallel and perpendicular to the crystallographic *c*-direction are shown. The critical current densities at 4.2 K and an applied magnetic field of 9 T parallel and perpendicular to the *c*-direction are 0.12 and 0.2 MA/cm<sup>2</sup>, respectively. This anisotropy with respect to the direction of the applied magnetic field is less pronounced than in conductors coated with REBa<sub>2</sub>Cu<sub>3</sub>O<sub>7</sub> (RE: rare earth element). The *j<sub>c</sub>* data of the BaFe<sub>2</sub>(As, P)<sub>2</sub> film at temperatures of 4.2, 10, and 20 K indicate that the dependence on the applied magnetic field at 20 K is much more pronounced than at 10 or 4.2 K. The high critical current densities and the weak field dependence at low temperatures suggest that the iron-based superconductors show promise in the generation of extremely high magnetic fields. Because of the very short coherence length along the crys-

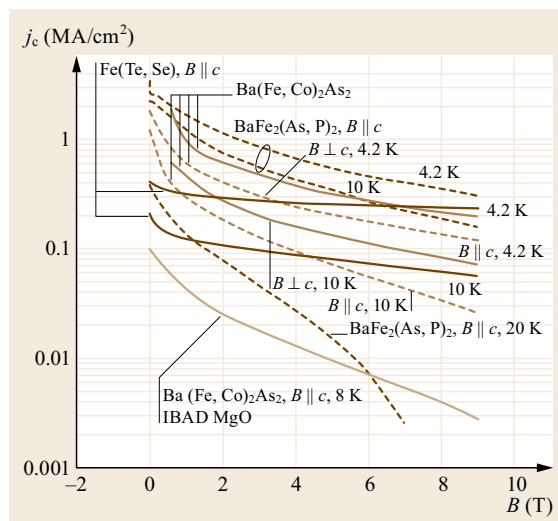


**Fig. 50.35** Critical current density versus field in Fe(Te,Se) [50.177], Ba(Fe, Co)<sub>2</sub>As<sub>2</sub> [50.178], BaFe<sub>2</sub>(As, P)<sub>2</sub> [50.179], and IBAD-MgO/Ba(Fe, Co)<sub>2</sub>As<sub>2</sub> films [50.180]

tallographic *c*-direction, they may show a weak-link behavior of the grain boundaries similar to the cuprates. Several research groups [50.170, 181–186] have studied the intergrain and the intragrain critical current densities in iron-based superconductors. Evidence for intergrain critical current densities much smaller than the intragrain *j<sub>c</sub>* has been found. However, the large difference between the two is caused partly by the wetting of the grain boundaries with FeAs. The extent to which the observed reduction of the intergrain *j<sub>c</sub>* is caused by an intrinsic weak-link problem needs to be clarified.

## 50.7 Summary

The cuprate high-temperature superconductors are characterized by layered crystal structures. Conductive CuO<sub>2</sub> layers in the crystallographic *ab*-planes are a common feature of all cuprate superconductors. Along the *c*-direction, conducting copper oxide blocks and insulating charge-carrier reservoirs alternate. As a consequence, the physical properties of cuprate superconductors are strongly anisotropic.

The critical temperature as well as the other physical properties depends considerably on the charge-carrier concentration. The maximum critical temperature is typically reached for a carrier concentration of 0.18 holes per CuO<sub>2</sub>. Furthermore, the highest *T<sub>c</sub>* of optimally doped cuprate superconductors is typically reached in

compounds with three or four CuO<sub>2</sub> layers in the CuO<sub>2</sub> blocks. The highest known critical temperature of 135 K at ambient pressure was achieved in Hg-1223.

The cuprate superconductors are close to a metal–insulator transition. The d-wave symmetry of the energy gap and the existence of a pseudogap above *T<sub>c</sub>*, especially in under-doped cuprate superconductors, suggest that the pairing mechanism of the electrons is different from that in metallic superconductors. Furthermore, only a weak isotope effect has been observed in the cuprates, which again suggests that the electron pairing is not phonon mediated.

Extremely short coherence lengths and low carrier concentrations seem to be responsible for the weak-link

**Table 50.9** Physical properties of various iron-based superconductors

Compound	Parameter	Value	Comments	Reference
<b>Critical temperatures</b>				
LaOFeP	$T_c$ (K)	$\approx 4$	P analog to LaOFeAs	[50.30]
La <sub>0.89</sub> F <sub>0.11</sub> FeAs	$T_c$ (K)	26	O partly replaced by F	[50.16]
La <sub>0.87</sub> Sr <sub>0.13</sub> OFeAs	$T_c$ (K)	25	La partly replaced by Sr	[50.151]
SmO <sub>0.74</sub> F <sub>0.26</sub> FeAs	$T_c$ (K)	58.1	O partly replaced by F	[50.34]
SmO(Fe <sub>0.9</sub> Co <sub>0.1</sub> )As	$T_c$ (K)	15.2	Fe partly replaced by Co	[50.152]
CeO <sub>0.84</sub> F <sub>0.16</sub> FeAs	$T_c$ (K)	41	O partly replaced by F	[50.153]
NdO <sub>0.75</sub> F <sub>0.25</sub> FeAs	$T_c$ (K)	55	O partly replaced by F	[50.154]
NdO <sub>0.85</sub> FeAs	$T_c$ (K)	46	Oxygen deficiency	[50.155]
GdO <sub>0.85</sub> FeAs	$T_c$ (K)	53.5	Oxygen deficiency	[50.156]
Gd <sub>0.8</sub> Th <sub>0.2</sub> OFeAs	$T_c$ (K)	56	Gd partly replaced by Th	[50.144]
DyO <sub>0.9</sub> F <sub>0.1</sub> FeAs	$T_c$ (K)	45	O partly replaced by F	[50.157]
LiFeAs	$T_c$ (K)	$\approx 18$		[50.147]
NaFeAs	$T_c$ (K)	12–25		[50.147]
Ba <sub>0.6</sub> K <sub>0.4</sub> Fe <sub>2</sub> As <sub>2</sub>	$T_c$ (K)	38	Ba partly replaced by K	[50.148]
Sr <sub>0.6</sub> K <sub>0.4</sub> Fe <sub>2</sub> As <sub>2</sub>	$T_c$ (K)	38	Sr partly replaced by K	[50.148]
Ba(Fe <sub>0.8</sub> Co <sub>0.2</sub> ) <sub>2</sub> As <sub>2</sub>	$T_c$ (K)	22	Co doping in FeAs layers	[50.148]
$\alpha$ - FeSe	$T_c$ (K)	8–27		[50.148]
Fe(Se <sub>0.5</sub> Te <sub>0.5</sub> )	$T_c$ (K)	$\approx 15.5$	Se partly replaced by Te	[50.148]
Fe(Se <sub>0.8</sub> S <sub>0.2</sub> )	$T_c$ (K)	$\approx 15.5$	Se partly replaced by S	[50.147]
Fe(Te <sub>0.8</sub> S <sub>0.2</sub> )	$T_c$ (K)	10	Te partly replaced by S	[50.147]
<b>Crystal structures and lattice parameters</b>				
LaOFeAs	$a$ (nm)	0.4039	Tetragonal (P4/nmm)	[50.158]
	$c$ (nm)	0.8742		
LaO <sub>0.8</sub> F <sub>0.2</sub> FeAs	$a$ (nm)	0.4030	Tetragonal (P4/nmm)	[50.158]
	$c$ (nm)	0.8716		
SmOFeAs	$a$ (nm)	0.3940	Tetragonal (P4/nmm)	[50.159]
	$c$ (nm)	0.8501		
SmO <sub>0.85</sub> F <sub>0.15</sub> FeAs	$a$ (nm)	0.3932	Tetragonal (P4/nmm)	[50.159]
	$c$ (nm)	0.8490		
BaFe <sub>2</sub> As <sub>2</sub>	$a$ (nm)	0.3964	Tetragonal (I4/mmm)	[50.160]
	$c$ (nm)	1.3022		
BaFe <sub>1.87</sub> Co <sub>0.13</sub> As <sub>2</sub>	$a$ (nm)	0.3963	Tetragonal (I4/mmm)	[50.160]
	$c$ (nm)	1.2991		
LiFeAs	$a$ (nm)	0.3791	Tetragonal (P4/nmm)	[50.161]
	$c$ (nm)	0.6364		
<b>Superconducting energy gaps</b>				
LaO <sub>0.9</sub> F <sub>0.1–<math>\delta</math></sub> FeAs	$\Delta$ (meV)	$3.9 \pm 0.7$	$T_c = 27$ K, $2\Delta/T_c = 3.35$	[50.162]
SmO <sub>0.8</sub> F <sub>0.2</sub> FeAs	$\Delta$ (meV)	$6.45 \pm 0.25$	$T_c = 51.2$ K, $2\Delta/T_c = 2.95$	[50.163]
(2 gaps)	$\Delta$ (meV)	$16.6 \pm 1.6$	$T_c = 51.2$ K, $2\Delta/T_c = 7.65$	
Ba <sub>0.6</sub> K <sub>0.4</sub> Fe <sub>2</sub> As <sub>2</sub>	$\Delta$ (meV)	6	$T_c = 37$ K, $2\Delta/T_c = 3.76$	[50.164]
(2 gaps)	$\Delta$ (meV)	12	$T_c = 37$ K, $2\Delta/T_c = 7.53$	
LiFeAs (single gap)	$\Delta$ (meV)	$3 \pm 0.2$	$T_c = 17$ K, $2\Delta/T_c = 4.1$	[50.165]
<b>Upper critical fields</b>				
LaO <sub>0.9</sub> F <sub>0.1–<math>\delta</math></sub> FeAs	$B_{c2}$ (T)	56	$T = 0$ , $T_c = 28.9$ K	[50.166]
SmO <sub>0.65</sub> F <sub>0.35</sub> FeAs	$B_{c2}$ (T)	$\approx 120$	$T = 0$ , $T_c = 52$ K	[50.167]
CeO <sub>0.9</sub> F <sub>0.1</sub> FeAs	$B_{c2}$ (T)	94	$T = 0$ , $T_c = 38.4$ K	[50.168]
Ba <sub>0.6</sub> K <sub>0.4</sub> Fe <sub>2</sub> As <sub>2</sub>	$B_{c2}$ (T)	75	$B_{c2}^{ab}/B_{c2}^c \approx 1-3$	[50.149]
(Ba, K)Fe <sub>2</sub> As <sub>2</sub>	$B_{c2}$ (T)	70	$B_{c2}^{ab}/B_{c2}^c \approx 1.4$ , $T_c = 28$ K	[50.169]
Fe(Te, Se)	$B_{c2}$ (T)	87	$T = 0$	[50.148]

Table 50.9 (continued)

Compound	Parameter	Value	Comments	Reference
<b>Characteristic length scales</b>				
LaO <sub>0.89</sub> F <sub>0.11</sub> FeAs	$\xi_{ab}(0)$ (nm)	5	Coherence length	[50.170]
	$\xi_c(0)$ (nm)	1.2		
LaO <sub>0.9</sub> F <sub>0.1</sub> FeAs	$\lambda_{ab}(0)$ (nm)	254	Penetration depth	[50.171]
NdO <sub>0.82</sub> F <sub>0.18</sub> FeAs	$\xi_{ab}(0)$ (nm)	3.1	Coherence length	[50.172]
	$\xi_c(0)$ (nm)	0.78		
SmO <sub>0.9</sub> F <sub>0.1</sub> FeAs	$\lambda_{ab}(0)$ (nm)	205	Penetration depth	[50.173]
Ba <sub>0.6</sub> K <sub>0.4</sub> Fe <sub>2</sub> As <sub>2</sub>	$\xi_{ab}(0)$ (nm)	1.25	Coherence length	[50.172]
	$\xi_c(0)$ (nm)	0.45		
	$\lambda_{ab}(0)$ (nm)	125	Penetration depth	
	$\lambda_c(0)$ (nm)	304		
SrFe <sub>1.75</sub> Co <sub>0.25</sub> As <sub>2</sub>	$\lambda_{ab}(0)$ (nm)	316	Penetration depth	[50.174]
	$\lambda_c(0)$ (nm)	870		
LiFeAs	$\xi_{ab}(0)$ (nm)	2–4	Coherence length	[50.165]
	$\lambda_{ab}(0)$ (nm)	210		
FeSe <sub>0.89</sub>	$\xi(0)$ (nm)	3.14	Coherence length	[50.175]
	$\lambda(0)$ (nm)	1008		
Fe(Se, Te)	$\xi_{ab}(0)$ (nm)	1.2	Coherence length	[50.176]
	$\xi_c(0)$ (nm)	0.35		

behavior of large-angle grain boundaries in the cuprate superconductors. To achieve transport critical current densities comparable to the intra-grain  $j_c$ , a biaxial texture is required.

Since the discovery of superconductivity above 50 K in the iron pnictides, the cuprates are no longer the only class of high-temperature superconductors. In the iron pnictides, layers of FeAs alternate with layers of REO, alkaline earth or alkali ions, which act as charge-carrier reservoirs resembling those in the cuprate superconductors. As in the cuprates, the superconducting state is close to an antiferromagnetic state. However, the parent compounds of the iron-pnictide superconductors are metals and not Mott insulators as in the case of the cuprates. Because of their very high upper critical fields, the iron-based superconductors are potential high field superconductors.

The metallic intermediate-temperature superconductor MgB<sub>2</sub> may have applications in spite of its

moderate critical temperature of 39 K, because of its simpler chemistry and the fact that its grain boundaries do not act as weak links. The observation of a pronounced boron isotope effect suggests that MgB<sub>2</sub> is a conventional BCS superconductor. The anisotropy of the physical properties of MgB<sub>2</sub> is less pronounced than that of the cuprate superconductors.

The maximum operation fields of MgB<sub>2</sub>, cuprate and iron-based superconductors are limited by the irreversibility line, which is well below the upper critical field. The existence of an irreversibility line may be caused by thermally activated depinning or flux-line lattice melting.

**Acknowledgments.** The author wishes to thank P. Bruzzone for his support and encouragement. The careful reviewing and many constructive suggestions on the manuscript by J. F. Crawford are especially appreciated.

## References

- |      |   |       |   |
|------|---|-------|---|
| 50.1 | R. de Bruyn Ouboter: IEEE Trans. Mag. <b>23</b> , 355 (1987)                  | 50.7  | I. Giaever: Phys. Rev. Lett. <b>5</b> , 464 (1960)  |
| 50.2 | W. Meissner, R. Ochsenfeld: Naturwissenschaften <b>21</b> , 787 (1933)        | 50.8  | R. Doll, M. Näbauer: Phys. Rev. Lett. <b>7</b> , 51 (1961)                                  |
| 50.3 | F. London, H. London: Physica <b>2</b> , 341 (1935)                           | 50.9  | B.S. Deaver Jr., W.M. Fairbank: Phys. Rev. Lett. <b>7</b> , 43 (1961)                       |
| 50.4 | J. Bardeen, L.N. Cooper, J.R. Schrieffer: Phys. Rev. <b>106</b> , 162 (1957)  | 50.10 | B.D. Josephson: Phys. Lett. <b>1</b> , 251 (1962)   |
| 50.5 | J. Bardeen, L.N. Cooper, J.R. Schrieffer: Phys. Rev. <b>108</b> , 1175 (1957) | 50.11 | R.C. Jaklevic, J. Lambe, J.E. Mercereau, A.H. Silver: Phys. Rev. A <b>140</b> , 1628 (1965) |
| 50.6 | I. Giaever: Phys. Rev. Lett. <b>5</b> , 147 (1960)                            | 50.12 | J.G. Bednorz, K.A. Müller: Z. Phys. B <b>64</b> , 189 (1986)                                |
|      |   | 50.13 | A. Schilling, M. Cantoni, J.D. Guo, H.R. Ott: Nature <b>363</b> , 56 (1993)                 |

- 50.14 J.J. Capponi, J.L. Tholence, C. Chailout, M. Marezio, P. Bordet, J. Chenavas, S.M. Loureiro, E.V. Antipov, E. Kopnina, M.F. Gorius, M. Nunez-Regueiro, B. Souletie, P. Radaelli, F. Gerhards: *Physica C* **235–240**, 146 (1994)
- 50.15 J. Nagamatsu, N. Nakagawa, T. Muranaka, Y. Zenitani, J. Akimitsu: *Nature* **410**, 63 (2001)
- 50.16 Y. Kamihara, T. Watanabe, M. Hirano, H. Hosono: *J. Am. Chem. Soc.* **130**, 3296 (2008)
- 50.17 L.R. Testardi, J.H. Wernick, W.A. Royer: *Solid State Commun.* **15**, 1 (1974)
- 50.18 J.R. Gavaler, M.A. Janocko, C.K. Jones: *J. Appl. Phys.* **45**, 3009 (1974)
- 50.19 J.F. Schooley, W.R. Hosler, M.L. Cohen: *Phys. Rev. Lett.* **12**, 474 (1964)
- 50.20 A.W. Sleight, J.L. Gillson, P.E. Bierstedt: *Solid State Commun.* **17**, 27 (1975)
- 50.21 M.K. Wu, J.R. Ashburn, C.J. Torng, P.H. Hor, R.L. Meng, L. Gao, Z.J. Huang, Y.Q. Wang, C.W. Chu: *Phys. Rev. Lett.* **58**, 908 (1987)
- 50.22 D. Jérôme, A. Mazaud, M. Ribault, K. Bechgaard: *J. Phys. Lett.* **41**, 195 (1980)
- 50.23 K. Oshima, H. Urayama, H. Yamochi, G. Saito: *Physica C* **153–155**, 1148 (1988)
- 50.24 J.M. Williams, A.J. Schultz, U. Geiser, K.D. Carlson, A.M. Kini, H.H. Wang, W.-K. Kwok, M.-H. Whangbo, J.E. Schirber: *Science* **252**, 1501 (1991)
- 50.25 A.F. Hebard, M.J. Rosseinsky, R.C. Haddon, D.W. Murphy, S.H. Glarum, T.T.M. Palstra, A.P. Ramirez, A.R. Kortan: *Nature* **350**, 600 (1991)
- 50.26 K. Lüders: *Phys. Bl.* **50**, 166 (1994)
- 50.27 T.T.M. Palstra, O. Zhou, Y. Iwasa, P.E. Sulewski, R.M. Fleming, B.R. Zegarski: *Solid State Commun.* **93**, 327 (1995)
- 50.28 Y. Kamihara, H. Hiramatsu, M. Hirano, R. Kawamura, H. Yanagi, T. Kamiya, H. Hosono: *J. Am. Chem. Soc.* **128**, 10012 (2006)
- 50.29 K.-W. Yeh, T.-W. Huang, Y.-L. Huang, T.K. Chen, F.-C. Hsu, P.M. Wu, Y.-C. Lee, Y.-Y. Chu, C.-L. Chen, J.-Y. Luo, D.-C. Yan, M.K. Wu: *Europhys. Lett.* **84**, 37002 (2008)
- 50.30 M. Rotter, M. Tegel, D. Johrendt: *Phys. Rev. Lett.* **101**, 107006 (2008)
- 50.31 Z.-A. Ren, G.-C. Che, X.-L. Dong, J. Yang, W. Lu, W. Yi, X.-L. Shen, Z.-C. Li, L.-L. Sun, F. Zhou, Z.-X. Zhao: *Europhys. Lett.* **83**, 17002 (2008)
- 50.32 G. Wu, Y.L. Xie, H. Chen, M. Zhong, R.H. Liu, B.C. Shi, Q.J. Li, X.F. Wang, T. Wu, Y.J. Yan, J.J. Ying, X.H. Chen: *J. Phys. Condens. Matter* **21**, 142203 (2009)
- 50.33 C. Wang, Z. Gao, L. Wang, Y. Qi, D. Wang, C. Yao, Z. Zhang, Y. Ma: *Supercond. Sci. Technol.* **23**, 55002 (2010)
- 50.34 M. Fujioka, S.J. Denholme, T. Ozaki, H. Okazaki, K. Deguchi, S. Demura, H. Hara, T. Watanabe, H. Takeya, T. Yamaguchi, H. Kumakura, Y. Takano: *Supercond. Sci. Technol.* **26**, 085023 (2013)
- 50.35 T.R. Strobridge: *IEEE Trans. Nucl. Sci.* **16**, 1104 (1969)
- 50.36 W.-J. Yeh, L. Chen, F. Xu, B. Bi, P. Yang: *Phys. Rev. B* **36**, 2414 (1987)
- 50.37 F.J. Kedves, S. Mészáros, K. Vad, G. Halász, B. Keszei, L. Mihály: *Solid State Commun.* **63**, 991 (1987)
- 50.38 D.J. Quinn, W.B. Ittner: *J. Appl. Phys.* **33**, 748 (1962)
- 50.39 R. Wesche: *High-Temperature Superconductors: Materials, Properties, and Applications* (Kluwer Academic, Boston 1998)
- 50.40 H. Fröhlich: *Phys. Rev.* **79**, 845 (1950)
- 50.41 J. Bardeen: *Phys. Rev.* **80**, 567 (1950)
- 50.42 C.P. Poole, H.A. Farach, R.J. Creswick: *Superconductivity* (Academic, San Diego 1995)
- 50.43 C.A. Reynolds, B. Serin, W.H. Wright, L.B. Nesbitt: *Phys. Rev.* **78**, 487 (1950)
- 50.44 E. Maxwell: *Phys. Rev.* **78**, 477 (1950)
- 50.45 B. Serin, C.A. Reynolds, C. Lohman: *Phys. Rev.* **86**, 162 (1952)
- 50.46 J.W. Garland: *Phys. Rev. Lett.* **11**, 114 (1963)
- 50.47 W. Buckel: *Supraleitung* (VCH, Weinheim 1993)
- 50.48 T.P. Orlando, K.A. Delin: *Foundations of Applied Superconductivity* (Addison-Wesley, Reading 1991)
- 50.49 G. Sparn, J.D. Thompson, R.L. Whetten, S.-M. Huang, R.B. Kaner, F. Diederich, G. Grüner, K. Holczer: *Phys. Rev. Lett.* **68**, 1228 (1992)
- 50.50 C. Renner, I. Maggio-Aprile, Ø. Fischer: *Phys. Bl.* **54**, 427 (1998)
- 50.51 C. Renner, B. Revaz, J.-Y. Genoud, K. Kadowaki, Ø. Fischer: *Phys. Rev. Lett.* **80**, 149 (1998)
- 50.52 Z.A. Xu, N.P. Ong, Y. Wang, T. Takeshita, S. Uchida: *Nature* **406**, 486 (2000)
- 50.53 N.E. Hussey: Normal state transport properties. In: *Handbook of High-Temperature Superconductivity: Theory and Experiment*, ed. by J.R. Schrieffer, J.S. Brooks (Springer, New York 2007)
- 50.54 J.-H. Ma, Z.-H. Pan, F.C. Niestemski, M. Neupane, Y.-M. Xu, P. Richard, K. Nakayama, T. Sato, T. Takahashi, H.-Q. Luo, L. Fang, H.-H. Wen, Z. Wang, H. Ding, V. Madhavan: *Phys. Rev. Lett.* **101**, 207002 (2008)
- 50.55 J. Orenstein, A.J. Millis: *Science* **288**, 468 (2000)
- 50.56 J.M. Tranquada, B.J. Sternlieb, J.D. Axe, Y. Nakamura, S. Uchida: *Nature* **375**, 561 (1995)
- 50.57 R. Beyers, G. Lim, E.M. Engler, R.J. Savoy, T.M. Shaw, T.R. Dinger, W.J. Gallagher, R.L. Sandstrom: *Appl. Phys. Lett.* **50**, 1918 (1987)
- 50.58 R.J. Cava, B. Batlogg, R.B. van Dover, D.W. Murphy, S. Sunshine, T. Siegrist, J.P. Remeika, E.A. Rietman, S. Zahurak, G.P. Espinosa: *Phys. Rev. Lett.* **58**, 1676 (1987)
- 50.59 A. Fukuoka, A. Tokiwa-Yamamoto, M. Itoh, R. Usami, S. Adachi, H. Yamauchi, K. Tanabe: *Physica C* **265**, 13 (1996)
- 50.60 T. Schweizer, R. Müller, L.J. Gauckler: *Physica C* **225**, 143 (1994)
- 50.61 R. Hott, H. Rietschel, M. Sander: *Phys. Bl.* **48**, 355 (1992)
- 50.62 A. Maignan, C. Martin, M. Huve, J. Provost, M. Hervieu, C. Michel, B. Raveau: *Physica C* **170**, 350 (1990)
- 50.63 A. Maignan, C. Martin, V. Hardy, C. Simon, M. Hervieu, B. Raveau: *Physica C* **219**, 407 (1994)
- 50.64 J.J. Capponi, E.M. Kopnin, S.M. Loureiro, E.V. Antipov, E. Gautier, C. Chailout, B. Souletie, M. Brunner, J.L. Tholence, M. Marezio: *Physica C*

- 256, 1 (1996)
- 50.65 L. Gao, Y.Y. Xue, F. Chen, Q. Xiong, R.L. Meng, D. Ramirez, C.W. Chu, J.H. Eggert, H.K. Mao: *Phys. Rev. B* **50**, 4260 (1994)
- 50.66 N. Watanabe, K. Fukamachi, Y. Ueda, K. Tsushima, A.M. Balbashov, T. Nakanishi, N. Môri: *Physica C* **235–240**, 1309 (1994)
- 50.67 J.-P. Locquet, J. Perret, J. Fompeyrine, E. Mächler, J.W. Seo, G. van Tendeloo: *Nature* **394**, 453 (1998)
- 50.68 M. Tinkham: *Physica C* **235–240**, 3 (1994)
- 50.69 A.J. Panson, G.R. Wagner, A.I. Braginski, J.R. Gavaler, M.A. Janocko, H.C. Pohl, J. Talvacchio: *Appl. Phys. Lett.* **50**, 1104 (1987)
- 50.70 D.W. Capone, D.G. Hinks, J.D. Jorgensen, K. Zhang: *Appl. Phys. Lett.* **50**, 543 (1987)
- 50.71 U. Welp, W.K. Kwok, G.W. Crabtree, K.G. Vandervoort, J.Z. Liu: *Phys. Rev. Lett.* **62**, 1908 (1989)
- 50.72 T.K. Worthington, W.J. Gallagher, T.R. Dinger: *Phys. Rev. Lett.* **59**, 1160 (1987)
- 50.73 C. Heinzel, C. Neumann, P. Ziemann: *Europhys. Lett.* **13**, 531 (1990)
- 50.74 D.-H. Wu, S. Sridhar: *Phys. Rev. Lett.* **65**, 2074 (1990)
- 50.75 M. Akamatsu, L.X. Chen, H. Ikeda, R. Yoshizaki: *Physica C* **235–240**, 1619 (1994)
- 50.76 D.R. Harshman, A.P. Mills: *Phys. Rev. B* **45**, 10684 (1992)
- 50.77 J.H. Kang, R.T. Kampwirth, K.E. Gray: *Appl. Phys. Lett.* **52**, 2080 (1988)
- 50.78 J.N. Li, K. Kadowaki, M.J.V. Menken, Y.K. Huang, K. Bakker, A.A. Menovsky, J.J.M. Franse: *Appl. Phys. A* **47**, 209 (1988)
- 50.79 L. Zhang, J.Z. Liu, R.N. Shelton: *Phys. Rev. B* **45**, 4978 (1992)
- 50.80 I. Matsubara, H. Tanigawa, T. Ogura, H. Yamashita, M. Kinoshita, T. Kawai: *Phys. Rev. B* **45**, 7414 (1992)
- 50.81 F. Shi, T.S. Rong, S.Z. Zhou, X.F. Wu, J. Du, Z.H. Shi, C.G. Cui, R.Y. Jin, J.L. Zhang, Q.Z. Ran, N.C. Shi: *Phys. Rev. B* **41**, 6541 (1990)
- 50.82 I. Matsubara, R. Funahashi, K. Ueno, H. Yamashita, T. Kawai: *Physica C* **256**, 33 (1996)
- 50.83 M. Hasegawa, K. Izawa, A. Shibata, Y. Matsuda: *Physica C* **377**, 459 (2002)
- 50.84 G. Triscone, A. Junod, R.E. Gladyshevskii: *Physica C* **264**, 233 (1996)
- 50.85 J. Hofer, J. Karpinski, M. Willemin, G.I. Meijer, E.M. Kopnin, R. Molinski, H. Schwer, C. Rossel, H. Keller: *Physica C* **297**, 103 (1998)
- 50.86 R. Usami, A. Fukuoka, H. Kubota, H. Yamauchi: *Physica C* **243**, 19 (1995)
- 50.87 G. Villard, A. Daignere, D. Pelloquin, A. Maignan: *Physica C* **314**, 196 (1999)
- 50.88 V. Vulcanescu, L. Fruchter, A. Bertinotti, D. Colson, G. Le Bras, J.-F. Marucco: *Physica C* **259**, 131 (1996)
- 50.89 T.T.M. Palstra, B. Batlogg, L.F. Schneemayer, J.V. Waszczak: *Phys. Rev. Lett.* **61**, 1662 (1988)
- 50.90 H. Kumakura, K. Togano, N. Tomita, E. Yanagisawa, S. Okayasu, Y. Kazumatu: *Physica C* **251**, 231 (1995)
- 50.91 V. Hardy, J. Provost, D. Groult, M. Hervieu, B. Raveau, S. Durčok, E. Pollert, J.C. Frison, J.P. Chaminade, M. Pouchard: *Physica C* **191**, 85 (1992)
- 50.92 L. Civale, A.D. Marwick, R. Wheeler, M.A. Kirk, W.L. Carter, G.N. Riley, A.P. Malozemoff: *Physica C* **208**, 137 (1993)
- 50.93 A. Schilling, R.A. Fisher, N.E. Phillips, U. Welp, D. Dasgupta, W.K. Kwok, G.W. Crabtree: *Nature* **382**, 791 (1996)
- 50.94 A. Junod, M. Roulin, J.-Y. Genoud, B. Revaz, A. Erb, E. Walker: *Physica C* **275**, 245 (1997)
- 50.95 M. Rupp, A. Gupta, C.C. Tsuei: *Appl. Phys. Lett.* **67**, 291 (1995)
- 50.96 L. Krusin-Elbaum, C.C. Tsuei, A. Gupta: *Nature* **373**, 679 (1995)
- 50.97 P. Schmitt, L. Schultz, G. Saemann-Ischenko: *Physica C* **168**, 475 (1990)
- 50.98 D. Dimos, P. Chaudhari, J. Mannhart, F.K. LeGoues: *Phys. Rev. Lett.* **61**, 219 (1988)
- 50.99 D. Dimos, P. Chaudhari, J. Mannhart: *Phys. Rev. B* **41**, 4038 (1990)
- 50.100 A. Schmehl, B. Goetz, R.R. Schulz, C.W. Schneider, H. Bielefeldt, H. Hilgenkamp, J. Mannhart: *Europhys. Lett.* **47**, 110 (1999)
- 50.101 A. Attenberger, J. Hänisch, B. Holzapfel, L. Schultz: *Physica C* **372–376**, 649 (2002)
- 50.102 J. Mannhart, H. Hilgenkamp: *Physica C* **317–318**, 383 (1999)
- 50.103 H. Hilgenkamp, J. Mannhart: *Appl. Phys. Lett.* **73**, 265 (1998)
- 50.104 R.A. Rao, Q. Gan, C.B. Eom, Y. Suzuki, A.A. McDaniel, J.W.P. Hsu: *Appl. Phys. Lett.* **69**, 3911 (1996)
- 50.105 H. Yamasaki, K. Endo, S. Kosaka, M. Umeda, S. Misawa, S. Yoshida, K. Kajimura: *IEEE Trans. Appl. Supercond.* **3**, 1536 (1993)
- 50.106 S.H. Yun, J.Z. Wu: *Appl. Phys. Lett.* **68**, 862 (1996)
- 50.107 D. Kumar, M. Sharon, R. Pinto, P.R. Apte, S.P. Pai, S.C. Purandare, L.C. Gupta, R. Vijayaraghavan: *Appl. Phys. Lett.* **62**, 3522 (1993)
- 50.108 T. Terashima, K. Shimura, Y. Bando, Y. Matsuda, A. Fujiyama, S. Komiyama: *Phys. Rev. Lett.* **67**, 1362 (1991)
- 50.109 J.-M. Triscone, Ø. Fischer, O. Brunner, L. Antognazza, A.D. Kent, M.G. Karkut: *Phys. Rev. Lett.* **64**, 804 (1990)
- 50.110 W. Si, H.-C. Li, X.X. Xi: *Appl. Phys. Lett.* **74**, 2839 (1999)
- 50.111 T. Sekitani, H. Sato, M. Naito, N. Miura: *Physica C* **378–381**, 195 (2002)
- 50.112 M.R. Eskildsen, M. Kugler, G. Levy, S. Tanaka, J. Jun, S.M. Kazakov, J. Karpinski, Ø. Fischer: *Physica C* **385**, 169 (2003)
- 50.113 R.S. Gonnelli, D. Daghero, G.A. Ummarino, V.A. Stepanov, J. Jun, S.M. Kazakov, J. Karpinski: *Phys. Rev. Lett.* **89**, 247004 (2002)
- 50.114 Z.-Z. Li, H.-J. Tao, Y. Xuan, Z.-A. Ren, G.-C. Che, B.-R. Zhao: *Phys. Rev. B* **66**, 064513 (2002)
- 50.115 S. Lee, Z.G. Khim, Y. Chong, S.H. Moon, H.N. Lee, H.G. Kim, B. Oh, E.J. Choi: *Physica C* **377**, 202 (2002)
- 50.116 P. Szabó, P. Samuely, J. Kačmarčík, T. Klein, J. Marcus, D. Fruchart, S. Miraglia, C. Marcenat, A.G.M. Jansen: *Phys. Rev. Lett.* **87**, 137005 (2001)
- 50.117 S.L. Bud'ko, G. Lapertot, C. Petrovic, C.E. Cunningham, N. Anderson, P.C. Canfield: *Phys. Rev. Lett.*

- 86, 1877 (2001)
- 50.118 D.G. Hinks, H. Claus, J.D. Jorgensen: *Nature* **411**, 457 (2001)
- 50.119 A. Gümbel, J. Eckert, G. Fuchs, K. Nenkov, K.-H. Müller, L. Schultz: *Appl. Phys. Lett.* **80**, 2725 (2002)
- 50.120 V. Braccini, L.D. Cooley, S. Patnaik, D.C. Larbalestier, P. Manfrinetti, A. Palenzona, A.S. Siri: *Appl. Phys. Lett.* **81**, 4577 (2002)
- 50.121 S.D. Bu, D.M. Kim, J.H. Choi, J. Giencke, E.E. Hellstrom, D.C. Larbalestier, S. Patnaik, L. Cooley, C.B. Eom, J. Lettieri, D.G. Schlom, W. Tian, X.Q. Pan: *Appl. Phys. Lett.* **81**, 1851 (2002)
- 50.122 T. Masui, S. Lee, A. Yamamoto, S. Tajima: *Physica C* **378–381**, 216 (2002)
- 50.123 Y. Wang, T. Plackowski, A. Junod: *Physica C* **355**, 179 (2001)
- 50.124 Z.X. Shi, A.K. Pradhan, M. Tokunaga, K. Yamazaki, T. Tamegai, Y. Takano, K. Togano, H. Kito, H. Ihara: *Physica C* **378–381**, 550 (2002)
- 50.125 M. Zehetmayer, M. Eisterer, J. Jun, S.M. Kazakov, J. Karpinski, A. Wisniewski, H.W. Weber: *Phys. Rev. B* **66**, 052505 (2002)
- 50.126 C. Ferdeghini, V. Ferrando, G. Grassano, W. Ramadan, V. Braccini, M. Putti, P. Manfrinetti, A. Palenzona: *Physica C* **372–376**, 1270 (2002)
- 50.127 Y. Ma, X. Zhang, S. Awaji, D. Wang, Z. Gao, G. Nishijima, K. Watanabe: *Supercond. Sci. Technol.* **20**, L5 (2007)
- 50.128 A. Matsumoto, H. Kitaguchi, H. Kumakura: *Supercond. Sci. Technol.* **21**, 065007 (2008)
- 50.129 Y. Eltsev, S. Lee, K. Nakao, N. Chikumoto, S. Tajima, N. Koshizuka, M. Murakami: *Physica C* **378–381**, 61 (2002)
- 50.130 F. Simon, A. Jánossy, T. Fehér, F. Murányi, S. Garaj, L. Forró, C. Petrovic, S.L. Bud'ko, G. Lapertot, V.G. Kogan, P.C. Canfield: *Phys. Rev. Lett.* **87**, 047002 (2001)
- 50.131 T. Takasaki, T. Ekino, T. Muranaka, H. Fujii, J. Akimitsu: *Physica C* **378–381**, 229 (2002)
- 50.132 F. Bouquet, R.A. Fisher, N.E. Phillips, D.G. Hinks, J.D. Jorgensen: *Phys. Rev. Lett.* **87**, 047001 (2001)
- 50.133 H.-J. Kim, W.N. Kang, E.-M. Choi, M.-S. Kim, K.H.P. Kim, S.-I. Lee: *Phys. Rev. Lett.* **87**, 087002 (2001)
- 50.134 J.M. An, W.E. Pickett: *Phys. Rev. Lett.* **86**, 4366 (2001)
- 50.135 H.J. Choi, D. Roundy, H. Sun, M.L. Cohen, S.G. Louie: *Nature* **418**, 758 (2002)
- 50.136 I.I. Mazin, V.P. Antropov: *Physica C* **385**, 49 (2003)
- 50.137 D.C. Larbalestier, L.D. Cooley, M.O. Rikel, A.A. Polyanskii, J. Jiang, S. Patnaik, X.Y. Cai, D.M. Feldmann, A. Gurevich, A.A. Squitieri, M.T. Naus, C.B. Eom, E.E. Hellstrom, R.J. Cava, K.A. Regan, N. Rogado, M.A. Hayward, T. He, J.S. Slusky, P. Khalifah, K. Inumaru, M. Haas: *Nature* **410**, 186 (2001)
- 50.138 K.H.P. Kim, W.N. Kang, M.-S. Kim, C.U. Jung, H.-J. Kim, E.-M. Choi, M.-S. Park, S.-I. Lee: *Physica C* **370**, 13 (2002)
- 50.139 W.N. Kang, H.-J. Kim, E.-M. Choi, K.H.P. Kim, S.-I. Lee: *Physica C* **378–381**, 1246 (2002)
- 50.140 S.L. Bud'ko, P.C. Canfield, V.G. Kogan: *Physica C* **382**, 85 (2002)
- 50.141 T. He, R.J. Cava, J.M. Rowell: *Appl. Phys. Lett.* **80**, 291 (2002)
- 50.142 M. Fujioka, S.J. Denholme, T. Ozaki, H. Okazaki, K. Deguchi, S. Demura, H. Hara, T. Watanabe, H. Takeya, T. Yamaguchi, H. Kumakura, Y. Takano: *Supercond. Sci. Technol.* **26**, 085023 (2013)
- 50.143 T. Nomura, S.W. Kim, Y. Kamihara, M. Hirano, P.V. Sushko, K. Kato, M. Takata, A.L. Shluger, H. Hosono: *Supercond. Sci. Technol.* **21**, 125028 (2008)
- 50.144 C. Wang, L. Li, S. Chi, Z. Zhu, Z. Ren, Y. Li, Y. Wang, X. Lin, Y. Luo, S. Jiang, X. Xu, G. Cao, Z. Xu: *Europhys. Lett.* **83**, 67006 (2008)
- 50.145 T. Yildirim: *Physica C* **469**, 425 (2009)
- 50.146 G. Wu, H. Chen, T. Wu, Y.L. Xie, Y.J. Yan, R.H. Liu, X.F. Wang, J.J. Ying, X.H. Chen: *J. Phys. Condens. Matter* **20**, 422201 (2008)
- 50.147 C.W. Chu, F. Chen, M. Gooch, A.M. Guloy, B. Lorenz, B. Lv, K. Sasmal, Z.J. Tang, J.H. Tapp, Y.Y. Zue: *Physica C* **469**, 326 (2009)
- 50.148 P.M. Aswathy, J.B. Anooja, P.M. Sarun, U. Syamaprasad: *Supercond. Sci. Technol.* **23**, 073001 (2010)
- 50.149 D. Johrendt, R. Pöttgen: *Physica C* **469**, 332 (2009)
- 50.150 S. Jiang, H. Xing, G. Xuan, C. Wang, Z. Ren, C. Feng, J. Dai, Z. Xu, G. Cao: *J. Phys. Condens. Matter* **21**, 382203 (2009)
- 50.151 H.-H. Wen, G. Mu, L. Fang, H. Yang, X. Zhu: *Europhys. Lett.* **82**, 17009 (2008)
- 50.152 Y. Qi, Z. Gao, L. Wang, D. Wang, X. Zhang, Y. Ma: *Supercond. Sci. Technol.* **21**, 115016 (2008)
- 50.153 G.F. Chen, Z. Li, D. Wu, G. Li, W.Z. Hu, J. Dong, P. Zheng, J.L. Luo, N.L. Wang: *Phys. Rev. Lett.* **100**, 247002 (2008)
- 50.154 A. Kursumovic, J.H. Durrell, S.K. Chen, J.L. MacManus-Driscoll: *Supercond. Sci. Technol.* **23**, 025022 (2010)
- 50.155 J.D. Moore, L.F. Cohen, Y. Yeshurun, A.D. Caplin, K. Morrison, K.A. Yates, C.M. McGilvery, J.M. Perkins, D.W. McComb, C. Trautmann, Z.A. Ren, J. Yang, W. Lu, X.L. Dong, Z.X. Zhao: *Supercond. Sci. Technol.* **22**, 125023 (2009)
- 50.156 J. Yang, Z.-C. Li, W. Lu, W. Yi, X.-L. Shen, Z.-A. Ren, G.-C. Che, X.-L. Dong, L.-L. Sun, F. Zhou, Z.-X. Zhao: *Supercond. Sci. Technol.* **21**, 082001 (2008)
- 50.157 M.A. McGuire, R.P. Hermann, A.S. Sefat, B.C. Sales, R. Jin, D. Mandrus, F. Grandjean, G.J. Long: *New J. Phys.* **11**, 025011 (2009)
- 50.158 C. Shekhar, S. Singh, P.K. Siwach, H.K. Singh, O.N. Srivastava: *Supercond. Sci. Technol.* **22**, 015005 (2009)
- 50.159 X.H. Chen, T. Wu, G. Wu, R.H. Liu, H. Chen, D.F. Fang: *Nature* **453**, 761 (2008)
- 50.160 K. Togano, Z. Gao, H. Taira, S. Ishida, K. Kihou, A. Iyo, H. Eisaki, A. Matsumoto, H. Kumakura: *Supercond. Sci. Technol.* **26**, 065003 (2013)
- 50.161 J.H. Tapp, Z. Tang, B. Lv, K. Sasmal, B. Lorenz, P.C.W. Chu, A.M. Guloy: *Phys. Rev. B* **78**, 060505(R) (2008)

- 50.162 L. Shan, Y. Wang, X. Zhu, G. Mu, L. Fang, C. Ren, H.-H. Wen: *Europhys. Lett.* **83**, 57004 (2008)
- 50.163 J. Karpinski, N.D. Zhigadlo, S. Katrych, Z. Bukowski, P. Moll, S. Weyeneth, H. Keller, R. Puzniak, M. Tortello, D. Daghero, R. Gonnelli, I. Maggio-Aprile, Y. Fasano, Ø. Fischer, K. Rogacki, B. Batlogg: *Physica C* **469**, 370 (2009)
- 50.164 H. Ding, P. Richard, K. Nakayama, K. Sugawara, T. Arakane, Y. Sekiba, A. Takayama, S. Souma, T. Sato, T. Takahashi, Z. Wang, X. Dai, Z. Fang, G.F. Chen, J.L. Luo, N.L. Wang: *Europhys. Lett.* **83**, 47001 (2008)
- 50.165 D.S. Inosov, J.S. White, D.V. Evtushinsky, I.V. Morozov, A. Cameron, U. Stockert, V.B. Zabolotnyy, T.K. Kim, A.A. Kordyuk, S.V. Borisenko, E.M. Forgan, R. Klingeler, J.T. Park, S. Wurmehl, A.N. Vasiliev, G. Behr, C.D. Dewhurst: *Phys. Rev. Lett.* **104**, 187001 (2010)
- 50.166 X. Zhu, H. Yang, L. Fang, G. Mu, H.-H. Wen: *Supercond. Sci. Technol.* **21**, 105001 (2008)
- 50.167 Z. Gao, L. Wang, Y. Qi, D. Wang, X. Zhang, Y. Ma, H. Yang, H. Wen: *Supercond. Sci. Technol.* **21**, 112001 (2008)
- 50.168 J. Prakash, S.J. Singh, S. Patnaik, A.K. Ganguli: *Physica C* **469**, 82 (2009)
- 50.169 H.Q. Yuan, J. Singleton, F.F. Balakirev, S.A. Baily, G.F. Chen, J.L. Luo, N.L. Wang: *Nature* **457**, 565 (2009)
- 50.170 A. Yamamoto, A.A. Polyanskii, J. Jiang, F. Kametani, C. Tarantini, F. Hunte, J. Jaroszynski, E.E. Hellstrom, P.J. Lee, A. Gurevich, D.C. Larbalestier, Z.A. Ren, J. Yang, X.L. Dong, W. Lu, Z.X. Zhao: *Supercond. Sci. Technol.* **21**, 095008 (2008)
- 50.171 H. Luetkens, H.-H. Klauss, R. Khasanov, A. Amato, R. Klingeler, I. Hellmann, N. Leps, A. Kondrat, C. Hess, A. Köhler, G. Behr, J. Werner, B. Büchner: *Phys. Rev. Lett.* **101**, 097009 (2008)
- 50.172 U. Welp, G. Mu, R. Xie, A.E. Koshelev, W.K. Kwok, H.Q. Luo, Z.S. Wang, P. Cheng, L. Fang, C. Ren, H.-H. Wen: *Physica C* **469**, 575 (2009)
- 50.173 C. Ren, Z.S. Wang, H.Q. Luo, H. Yang, L. Shan, H.H. Wen: *Physica C* **469**, 599 (2009)
- 50.174 R. Khasanov, A. Maisuradze, H. Maeter, A. Kwadrin, H. Luetkens, A. Amato, W. Schnelle, H. Rosner, A. Leithe-Jasper, H.-H. Klauss: *Phys. Rev. Lett.* **103**, 067010 (2009)
- 50.175 S.B. Zhang, X.D. Zhu, H.C. Lei, G. Li, B.S. Wang, L.J. Li, X.B. Zhu, Z.R. Yang, W.H. Song, J.M. Dai, Y.P. Sun: *Supercond. Sci. Technol.* **22**, 075016 (2009)
- 50.176 M. Putti, I. Pallecchi, E. Bellingeri, M.R. Cimberle, M. Tropeano, C. Ferdeghini, A. Palenzona, C. Tarantini, A. Yamamoto, J. Jiang, J. Jaroszynski, F. Kametani, D. Abaimov, A. Polyanskii, J.D. Weiss, E.E. Hellstrom, A. Gurevich, D.C. Larbalestier, R. Jin, B.C. Sales, A.S. Seif, M.A. McGuire, D. Mandrus, P. Cheng, Y. Jia, H.H. Wen, S. Lee, C.B. Eom: *Supercond. Sci. Technol.* **23**, 034003 (2010)
- 50.177 P. Mele, K. Matsumoto, K. Fujita, Y. Yoshida, T. Kiss, A. Ichinose, M. Mukaida: *Supercond. Sci. Technol.* **25**, 084021 (2012)
- 50.178 S. Trommler, J. Hänisch, V. Matias, R. Hühne, E. Reich, K. Iida, S. Haindl, L. Schultz, B. Holzapfel: *Supercond. Sci. Technol.* **25**, 084019 (2012)
- 50.179 S. Adachi, T. Shimode, M. Miura, N. Chikumoto, A. Takemori, K. Nakao, Y. Oshikubo, K. Tanabe: *Supercond. Sci. Technol.* **25**, 105015 (2012)
- 50.180 K. Iida, J. Hänisch, S. Trommler, V. Matias, S. Haindl, F. Kurth, I.L. del Pozo, R. Hühne, M. Kildszun, J. Engelmann, L. Schultz, B. Holzapfel: *Appl. Phys. Express* **4**, 013103 (2011)
- 50.181 S.-H. Hong, N.H. Lee, W.N. Kang, S.-G. Lee: *Supercond. Sci. Technol.* **27**, 055007 (2014)
- 50.182 E.S. Otabe, M. Kiuchi, S. Kawai, Y. Morita, J. Ge, B. Ni, Z. Gao, L. Wang, Y. Qi, X. Zhang, Y. Ma: *Physica C* **469**, 1940 (2009)
- 50.183 F. Kametani, A.A. Polyanskii, A. Yamamoto, J. Jiang, E.E. Hellstrom, A. Gurevich, D.C. Larbalestier, Z.A. Ren, J. Yang, X.L. Dong, W. Lu, Z.X. Zhao: *Supercond. Sci. Technol.* **22**, 015010 (2009)
- 50.184 M. Eisterer, M. Zehetmayer, H.W. Weber, J. Jiang, J.D. Weiss, A. Yamamoto, E.E. Hellstrom, D.C. Larbalestier, N.D. Zhigadlo, J. Karpinski: *Supercond. Sci. Technol.* **23**, 054006 (2010)
- 50.185 S. Haindl, M. Kildszun, A. Kauffmann, K. Nenkov, N. Kozlova, J. Freudenberger, T. Thersleff, J. Hänisch, J. Werner, E. Reich, L. Schultz, B. Holzapfel: *Phys. Rev. Lett.* **104**, 077001 (2010)
- 50.186 S.J. Singh, R. Beck, S. Wurmehl, C. Hess, B. Büchner: *Supercond. Sci. Technol.* **28**, 025006 (2015)